

## A Global Climatology of Surface Wind and Wind Stress Fields from Eight Years of QuikSCAT Scatterometer Data

CRAIG M. RISIEN AND DUDLEY B. CHELTON

*College of Oceanic and Atmospheric Sciences, and Cooperative Institute for Oceanographic Satellite Studies, Oregon State University, Corvallis, Oregon*

(Manuscript received 18 July 2007, in final form 9 April 2008)

### ABSTRACT

Global seasonal cycles of the wind and wind stress fields estimated from the 8-yr record (September 1999–August 2007) of wind measurements by the NASA Quick Scatterometer (QuikSCAT) are presented. While this atlas, referred to here as the Scatterometer Climatology of Ocean Winds (SCOW), consists of 12 variables, the focus here is on the wind stress and wind stress derivative (curl and divergence) fields. SCOW seasonal cycles are compared with seasonal cycles estimated from NCEP–NCAR reanalysis wind fields. These comparisons show that the SCOW atlas is able to capture small-scale features that are dynamically important to both the ocean and the atmosphere but are not resolved in other observationally based wind atlases or in NCEP–NCAR reanalysis fields. This is particularly true of the wind stress derivative fields in which topographic, SST gradient, and ocean current influences on surface winds are plainly visible. Discussions of five example regions are presented to highlight these seasonally recurring small-scale features. It is expected that the SCOW atlas will prove valuable to researchers conducting hydrographic and modeling studies.

### 1. Introduction

For the past 25 yr, ocean modelers and air-sea interaction researchers have relied heavily on observationally based wind climatologies such as the Hellerman and Rosenstein climatology (Hellerman and Rosenstein 1983, hereafter HR), the *Atlas of Surface Marine Data 1994* (ASMD94; Da Silva et al. 1994), and the National Oceanography Center flux climatology (Josey et al. 2002; previously known as the Southampton Oceanography Center flux climatology and referred to as NOC hereafter). Such climatologies are limited by poor spatial and temporal in situ coverage by buoys and ships alike. Even in areas where such observations exist, their distribution is highly variable in both time and space, and, as such, in situ data do not resolve spatial and temporal variability of global ocean winds except on large spatial scales and long time scales. Figures 1b,c show, respectively, the average number of ship observations for the months of December, January, and Feb-

ruary (DJF) and for June, July, and August (JJA) from 46 yr of International Comprehensive Ocean–Atmosphere Dataset (ICOADS) release 2.1 (Worley et al. 2005). These ship-based observations are heavily biased in favor of the Northern Hemisphere and along major shipping routes. This is particularly true for the austral winter months (JJA) when the sampling of the Southern Ocean is reduced to almost zero.

HR presented the first ship-based monthly climatology of wind stress and wind stress curl fields on a global  $2^\circ \times 2^\circ$  grid. Their atlas was based on over 35 million ship measurements taken over the 106-yr period 1870–1976. HR calculated wind stress using a drag coefficient that was subsequently considered to be unrealistically strong. The Working Group on Air-Sea Fluxes (WGASF 2000) showed that the scheme employed by HR leads to a drag coefficient that is about 25% greater than that generally accepted today. This overestimate of wind stress was also noted in studies by Harrison (1989), Chelton et al. (1990), and Gordon and Corry (1991). In addition to the bias arising from the choice of drag coefficient, the HR climatology is poorly sampled in the polar and subpolar regions of both hemispheres, where there were fewer than 500 observations per grid cell, equivalent to an average of about

*Corresponding author address:* Craig M. Risien, College of Oceanic and Atmospheric Sciences, 104 COAS Administration Building, Oregon State University, Corvallis, OR 97331-5503.  
E-mail: crisien@coas.oregonstate.edu

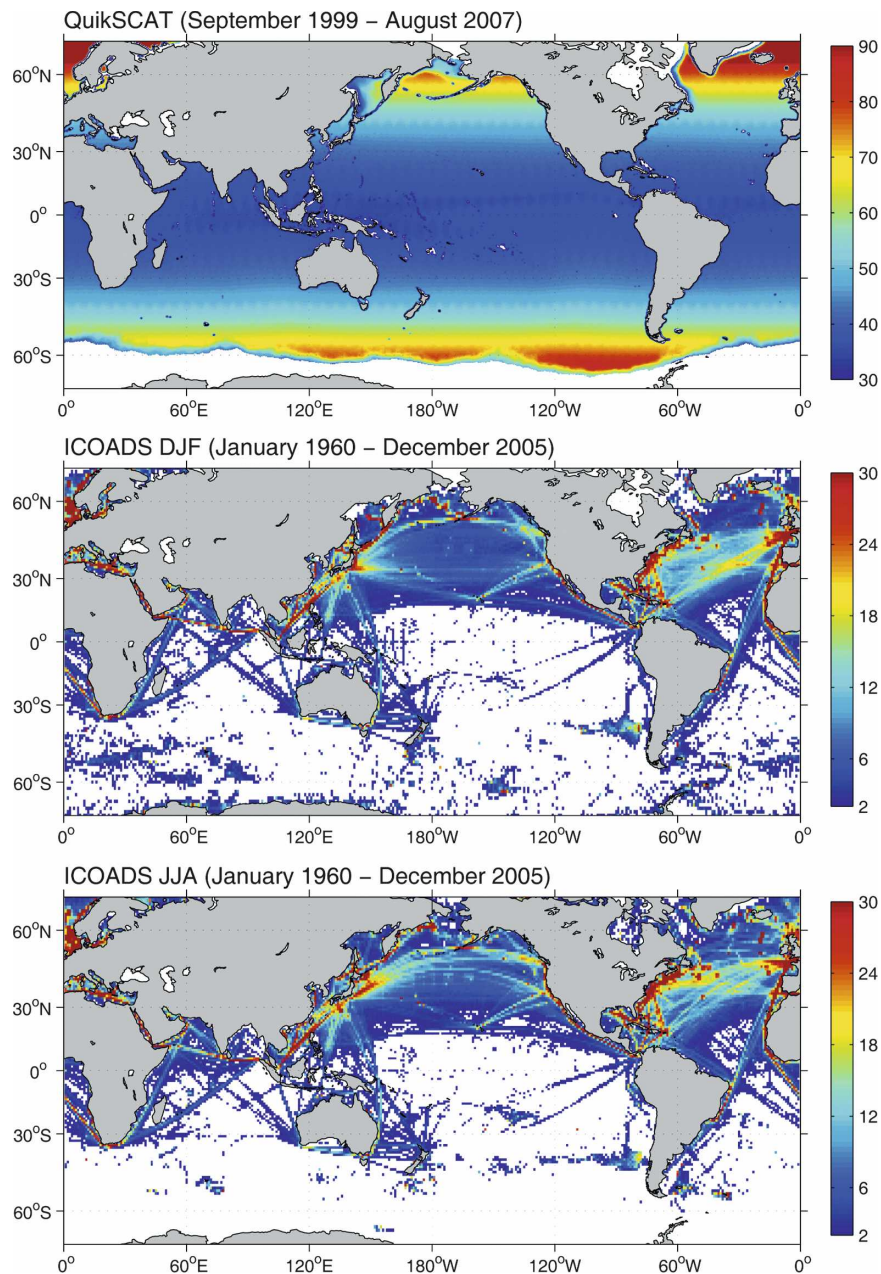


FIG. 1. (top) The average number of QuikSCAT observations per  $0.25^\circ \times 0.25^\circ$  grid cell per month for the 8-yr period September 1999 through August 2007. (middle) The average number of ICOADS observations per  $1^\circ \times 1^\circ$  grid cell per month for DJF for the 46-yr period 1960 through 2005. (bottom) The average number of ICOADS observations per  $1^\circ \times 1^\circ$  grid cell per month for JJA for the same 46-yr period. Grid cells with an average of less than two observations per month are shown in white. Note the Northern Hemisphere sampling bias. This is particularly true for the months of JJA.

4.7 observations per grid cell per year (see HR's Fig. 1). It is not surprising, then, that the standard error plots of mean zonal wind stress presented in HR show the largest errors in the poorly sampled regions poleward of about  $50^\circ$ .

*ASMD94* atlas presents monthly fields of zonal and meridional wind components, air and sea surface temperature, and sea level pressure on a global  $1^\circ \times 1^\circ$  grid. These fields are derived from the Comprehensive Ocean–Atmosphere Dataset release 1 (COADS)

(Woodruff et al. 1987). The majority of observations included in COADS were obtained from the ships of the Voluntary Observing Fleet. Observations from military ships, ocean weather ships, light ships, research vessels, buoys, and bathythermographs are also included in this historical collection. Although COADS includes observations as far back as 1854, the *ASMD94* climatology is based only on the years 1945 through 1989. As with HR, the majority of oceans are poorly sampled by the COADS dataset. This is particularly true of the tropical and Southern Hemisphere oceans. For the 38-yr period 1960–97, about 70% of grid cells within COADS are sampled less than twice per month (Risien and Chelton 2006).

The lack of observations over the Southern Ocean is also clear from the wind stress fields presented in the NOC climatology. Using wind stress estimates obtained from a modified version of the COADS release 1a (Woodruff et al. 1993) as well as metadata from WMO47 (WMO 1993), NOC presents monthly composites of zonal and meridional wind stress components on a  $1^\circ \times 1^\circ$  grid. These sea surface wind stress estimates are calculated by converting reported wind speeds to a neutral-stability wind at a height of 10 m above the sea surface using the flux-profile relations and transfer coefficients defined by Smith (1988, 1989), except that NOC adopts the 10-m neutral drag coefficient relationship of Smith (1980). The original NOC climatology based on the years 1980 through 1993 was recently extended to include the period 1994 through 2005. This 26-yr NOC dataset is the best *in situ* wind dataset presently available.

To assess the quality of ship-based wind climatologies, the RMS wind stress component differences between the 72 Quick Scatterometer (QuikSCAT) and NOC monthly fields over the 6-yr period September 1999–August 2005 are shown for the NOC  $1^\circ \times 1^\circ$  grid in the top two panels of Fig. 2. The RMS wind stress magnitude difference between QuikSCAT and NOC for the same 6-yr period is shown in the lower panel of Fig. 2. Over much of the world's oceans, the RMS differences between the two observationally based datasets fall between 0.01 and  $0.02 \text{ N m}^{-2}$ . Because of the existence of spurious features due to inadequate *in situ* sampling, the individual monthly fields in the NOC flux dataset have been masked to exclude the majority of the Southern Ocean.<sup>1</sup> Even in regions of the Southern Ocean that are not masked, the RMS differences between QuikSCAT and NOC are relatively high. In

the south Indian Ocean, for example, the zonal wind stress component and wind stress magnitude RMS differences exceed  $0.06 \text{ N m}^{-1.2}$ .

The better agreement between the QuikSCAT and NOC climatologies in the more well-sampled Northern Hemisphere and low- and midlatitude Southern Hemisphere regions gives a misleading impression of the quality of wind fields constructed from the NOC climatology. In particular, the ship-based observations do not resolve the small-scale features that are readily apparent in the QuikSCAT-based wind stress curl and divergence fields. The spatial high-pass filtering of the derivative operations of the curl and divergence emphasize these small-scale features, as shown in section 3. The wind stress curl is of particular interest because it is the primary forcing mechanism for large-scale ocean circulation. (The inadequacies of ship-based wind climatologies are clearly apparent from the wind stress curl fields in Fig. A1 of appendix A and Fig. 10 in section 3c.) Thus, while the NOC database provides long time series of winds in the well-sampled regions, the gridded fields are of questionable utility for ocean modeling applications.

The National Centers for Environmental Prediction (NCEP) and the European Centre for Medium-Range Weather Forecasts (ECMWF) operational numerical weather prediction models, which assimilate satellite observations of tropospheric temperature and humidity profiles, and *in situ* observations of tropospheric and surface winds and sea level pressure provide an alternative source for ocean surface wind stress estimates. These analyzed model wind fields are perhaps less susceptible to the spatial and temporal sampling issues that plague ship-based analyses; they are therefore able to provide full global coverage and temporal sampling, though with larger uncertainty in the poorly sampled regions of the World Ocean, in particular over the Southern Hemisphere. Moreover, the wind fields from the operational NCEP and ECMWF models are not able to resolve scales shorter than about 500 km (see Fig. 1 of Milliff et al. 2004; Fig. 1 of Chelton et al. 2006).

Trenberth et al. (1990, hereafter TLO) presented a wind stress climatology on a global  $2.5^\circ \times 2.5^\circ$  grid that was based on 7 yr (1980–86) of ECMWF operational model output. The TLO climatology was derived from vector averages of twice-daily wind stresses computed from 1000-mb winds. While TLO acknowledge that the

<sup>1</sup> See [ftp://ftp.noc.soton.ac.uk/pub/sxj/clim/matlab/noc\\_readme](ftp://ftp.noc.soton.ac.uk/pub/sxj/clim/matlab/noc_readme). Note that the Southern Ocean has not been masked in the monthly composite average fields in the NOC flux climatology.

<sup>2</sup> The swath-by-swath calculation of the derivative fields (curl and divergence) preserves the signals of each meteorological event and avoids introducing artifacts from differencing between grid points composed of averages of wind stress vectors over different sets of observation times.

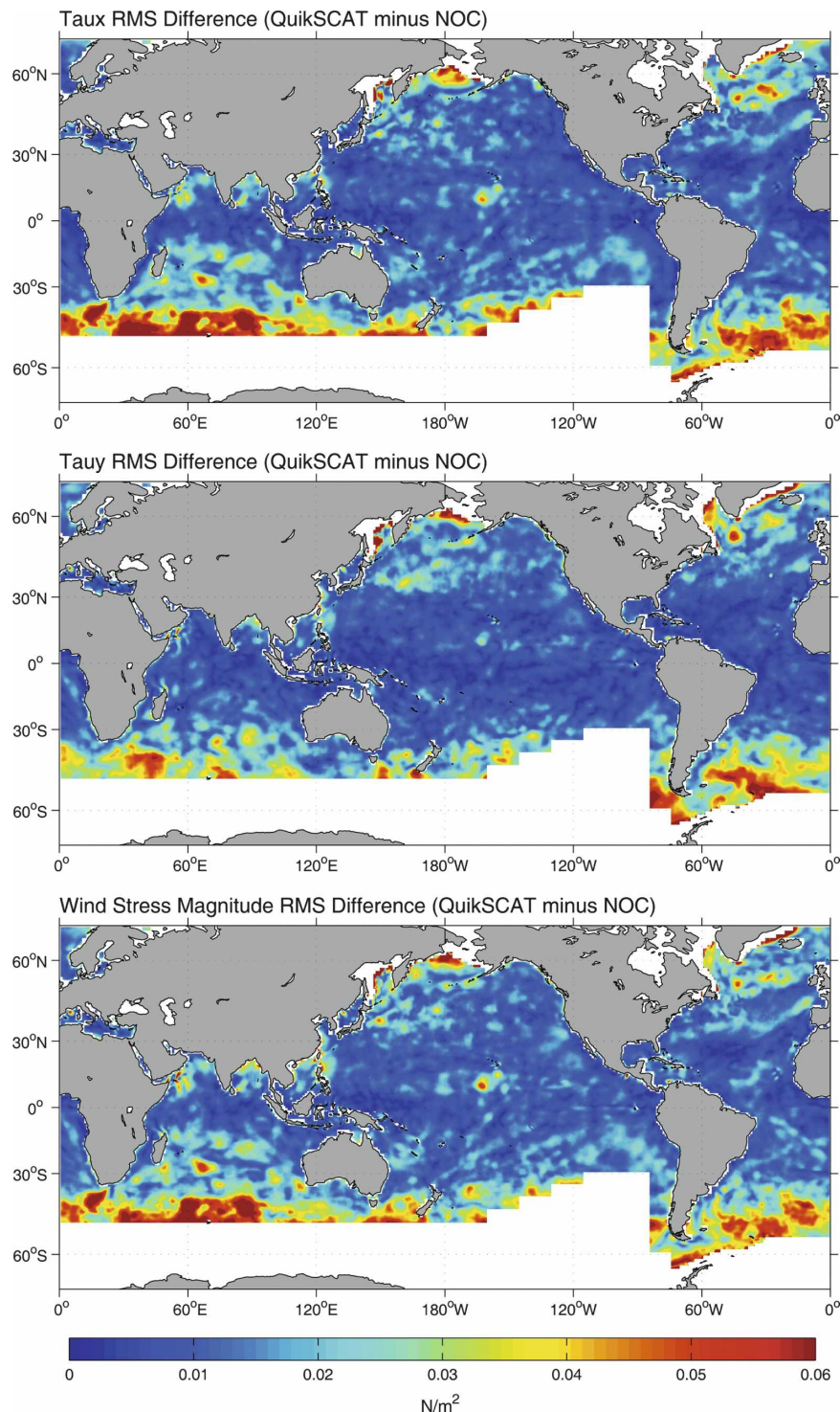


FIG. 2. (a), (b) Zonal and meridional RMS wind stress differences, respectively, between QuikSCAT and NOC monthly composite fields for the 6-yr period September 1999–August 2005. (c) The RMS wind stress magnitude difference between QuikSCAT and NOC for the same 6-yr period. Because of errors and the existence of spurious features, monthly composite NOC wind stress fields are masked south of about 45°S.

winds at the 1000-mb level are not generally expected to be equal to those at the surface, they cite Böttger (1982), who showed that ECMWF 1000-mb winds compare favorably with wind observations at ocean weather ship *Lima* ( $57^{\circ}\text{N}$ ,  $20^{\circ}\text{W}$ ), in support of their argument. Additional support for this argument appears to be provided by Janssen et al. (1989), who obtained accurate predictions in wave forecast models forced by 1000-mb ECMWF winds with no adjustment to 10-m winds. TLO therefore assumed the ECMWF 1000-mb winds to be equal to 10-m winds. This assumption was, however, shown by Mestas-Nuñez et al. (1994) to be questionable. Using 3 months (August–September 1978) of *Seasat-A* Satellite Scatterometer (SASS) data, Mestas-Nuñez et al. (1994) showed the TLO wind stresses to be systematically stronger than those measured by SASS by as much as 50%. The greatest differences were observed over the Southern Ocean where wind stress differences often exceeded  $0.06 \text{ N m}^{-2}$ . It is noteworthy that TLO found significantly stronger zonal wind stresses than HR over the Southern Ocean. TLO attribute this to inadequate sampling in the HR records, but the systematic bias in the TLO interpretation of 1000-mb winds as equivalent to 10-m winds is surely also a contributing factor.

While the ECMWF and NCEP operational models do provide global spatial coverage, they are limited in two ways. Relative to the QuikSCAT winds (Chelton and Freilich 2005), which have a resolution of about 25 km, the ECMWF and NCEP operational forecast models have grid spacings of about 35 km. The actual feature resolution in the model fields is about a factor of 10 coarser (Milliff et al. 2004; Chelton et al. 2006). The ECMWF (Gibson et al. 1997) and NCEP–NCAR (Kalnay et al. 1996; Kistler et al. 2001) reanalysis winds that are often used to force ocean models have even coarser grid spacings of  $2.5^{\circ}$  and about  $1.875^{\circ}$ , respectively, resulting in a feature resolution of about 1500 km (Milliff et al. 2004). The operational and reanalysis models are therefore not able to resolve small-scale wind features that are dynamically important to both the ocean and the atmosphere. Additionally, the accuracy of such models is limited by the model physics. TLO note, for example, that the ECMWF model was unable to adequately reproduce the convergent characteristics of the wind stress fields in the tropical Pacific. Moreover, Milliff and Morzel (2001) show that National Centers for Environmental Prediction (NCEP)–National Center for Atmospheric Research (NCAR) reanalysis surface wind fields contain evidence of spectral ringing throughout the global domain. This ringing is attributed to the inability of the spherical harmonic NCEP–NCAR model to represent abrupt transitions in mountain

topography with a truncated set of spectral modes. As shown later (bottom of Figs. 6, 8), this phenomenon is most pronounced in regions to the west and east of large topographic features such as the Andes (Milliff and Morzel 2001). The spectral ringing in the NCEP–NCAR reanalysis wind stress curl fields could lead to spurious artifacts in ocean models forced by these wind fields.

The HR and TLO climatologies continue to be used to force ocean models more than a decade after they were first published, despite their questionable accuracies noted above. Some recent examples include Mignone et al. (2006), Stuhne and Peltier (2006), Saenko et al. (2005), Urbano et al. (2006), Seidov and Haupt (2005), and O'Connor et al. (2005). There is clearly a need for an accurate, high-spatial-resolution, observationally based, truly global surface wind climatology. The 8-yr QuikSCAT Scatterometer Climatology of Ocean Winds (SCOW) presented here seeks to address this need.

In this paper, SCOW is not directly compared to previous climatologies, because of the inadequacies of past climatologies outlined above and the fact that the time periods for which past climatologies were calculated do not overlap with that of SCOW. SCOW is, however, evaluated against an NCEP–NCAR reanalysis climatology derived here using the methodology detailed in section 2d. NCEP–NCAR reanalysis fields were selected for comparison for two reasons. First, a consistent model methodology is used to calculate these reanalysis fields from January 1948 through the present. Second, NCEP–NCAR monthly composites of wind stress are readily available for the 8-yr period used to derive SCOW. The SCOW climatology consists of seasonal cycles of a number of variables including wind speed, wind speed squared, wind speed cubed, zonal and meridional wind components, wind curl (vorticity) and divergence, wind stress magnitude, zonal and meridional wind stress components, and wind stress curl and divergence (all of which are available for download at <http://cioss.coas.oregonstate.edu/scow>). In this study, we focus only on the wind stress and wind stress derivative fields.

## 2. Data and methods

### a. SeaWinds on QuikSCAT

On 19 June 2007, the SeaWinds scatterometer on board the QuikSCAT satellite celebrated its eighth year in orbit. The QuikSCAT mission was a “quick recovery” mission to fill the gap created by the unexpected loss of the National Aeronautics and Space Administration (NASA) Scatterometer (NSCAT) in June

1997 after only 9 months of operation due to a power failure on the *ADEOS-1* satellite. The QuikSCAT satellite operates in a sun-synchronous orbit, 803 km above the earth's surface. With an orbit period of 101 min, QuikSCAT is able to sample about 90% of the global oceans daily (Schlax et al. 2001). Figure 1a shows that this temporal sampling rate results in an average of about 30–50 observations per grid cell per month over most of the World Ocean, with more than 60 observations per month at latitudes poleward of about 50° latitude. As a result of antenna sidelobe contamination, standard QuikSCAT measurements cannot be obtained closer than about 30 km to land.

As summarized by Freilich et al. (1994) and Chelton and Freilich (2005), the SeaWinds scatterometer is a scanning microwave radar that measures electromagnetic backscatter from the wind-roughened ocean surface at multiple antenna look angles to infer surface wind stress magnitude and direction. The scatterometer is fundamentally a stress-measuring instrument. However, because of the inadequacy of the database of direct measurements of stress for calibration purposes, the radar backscatter is calibrated to the equivalent neutral-stability wind at a height of 10 m above the sea surface, that is, the wind  $\tilde{u}_{10}$  at a height of 10 m that would produce the observed wind stress if the atmosphere were neutrally stable.

The reason for presenting scatterometer winds as equivalent neutral-stability winds is that the database of direct measurements of stress is inadequate for developing a model function for converting scatterometer measurements of radar cross section directly to stress. It is straightforward, however, to convert buoy wind measurements to equivalent neutral-stability winds at 10 m using the Liu and Tang (1996) algorithm based on actual winds (measured at a known height above the sea surface) and air and sea surface temperature measured simultaneously by the buoy. A much larger database can thus be obtained for development of a model function relating radar cross section to equivalent neutral stability winds. Expressing scatterometer measurements as equivalent neutral stability winds has the added advantage of making scatterometer data useful for meteorological applications, which usually require wind rather than stress. The equivalent neutral stability wind at 10 m seldom differs from the actual winds at 10 m by more than a few tenths of a meter per second (Mears et al. 2001).

When compared with well-calibrated buoy observations that have been converted to 10-m equivalent neutral-stability winds, the accuracy of individual QuikSCAT observations is about  $0.75 \text{ m s}^{-1}$  in the along-wind direction and  $1.50 \text{ m s}^{-1}$  in the crosswind

direction (Chelton and Freilich 2005). Wind direction accuracy is a sensitive function of wind speed at low wind speeds but improves rapidly with increasing wind speed. For winds higher than about  $6 \text{ m s}^{-1}$ , the anisotropic component errors correspond to a directional accuracy of about  $14^\circ$  (Chelton and Freilich 2005).

Because QuikSCAT winds are archived as equivalent neutral-stability 10-m winds, conversion to stress using the bulk aerodynamic formula (see appendix B) is straightforward, requiring only the drag coefficient for neutrally stable conditions, regardless of the actual stability at the time of measurement. An advantage of the equivalent neutral-stability winds is thus that users can apply their preferred formulation of the neutral-stability drag coefficient. Here, we have used the modified Large and Pond neutral stability drag coefficient (see the appendix of Large et al. 1994), which is the formulation most commonly applied to scatterometer data. The vector wind stress, wind stress curl, and wind stress divergence were calculated on a swath-by-swath basis from all rain-free QuikSCAT wind measurements centered in each  $25 \text{ km} \times 25 \text{ km}$  bin.<sup>2</sup> Rain-contaminated cells were identified using the so-called multidimensional histogram-based (MUDH) algorithm (Hudleston and Stiles 2000; Stiles and Yueh 2002).

The QuikSCAT geophysical data record began on 15 July 1999. The 8-yr data record presented here extends from September 1999 through August 2007. The in-swath measurements were interpolated and smoothed onto a  $0.25^\circ$  latitude  $\times 0.25^\circ$  longitude grid using a loess smoother (Schlax et al. 2001) with a half-power filter cutoff wavelength of about 70 km, which is approximately equivalent to the filter cutoff of 40-km block averages. This smoothing and interpolation utilizes measurements within a circle with radius 70 km centered on each  $0.25^\circ$  grid point. Except in the intertropical convergence zone, rain-contaminated data usually consist of isolated measurement cells or small clusters of measurement cells. The 70-km smoothing thus fills in most of the rain-contaminated "holes" in the measurement swaths. As noted in Chelton et al. (2004), this mitigates the biases in the divergence and curl fields that arise if this hole filling is not applied (Milliff et al. 2004). The resulting gridded and smoothed stresses were then vector averaged monthly over the 8-yr data record. Monthly average wind stress curl and divergence measurements were computed on the  $0.25^\circ$  latitude  $\times 0.25^\circ$  longitude grid in the same manner as the monthly averaged wind stress fields.

The SCOW wind stress fields are clearly dependent on the specific formulation of the drag coefficient used in the bulk aerodynamic formula. As noted above, the modified Large and Pond drag coefficient used here is

the most commonly used formulation applied to scatterometer data. Other formulations that are sometimes used include the Smith (1980) drag coefficient in the NOC climatology and the Coupled Ocean–Atmosphere Response Experiment (COARE) version 3.0 drag coefficient described by Fairall et al. (2003). It is shown in appendix B that these formulations result in climatological monthly wind stress fields that are about 5% and 15% stronger, respectively, than are obtained based on the Large and Pond drag coefficient used here. Users who prefer the Smith (1980) or COARE 3.0 drag coefficients can accurately adjust the SCOW wind stress, wind stress curl, and wind stress divergence fields by multiplying them by factors of 1.05 and 1.15, respectively.

#### b. AMSR on EOS Aqua

The high-resolution QuikSCAT climatological average wind fields presented here contain many small-scale features that are highly correlated with the sea surface temperature (SST) field. This SST influence on the low-level wind field is shown in section 3d from comparisons with satellite measurements of SST from the Advanced Microwave Scanning Radiometer for Earth Observing System (EOS;AMSR-E) that was launched on 4 May 2002 aboard NASA's EOS *Aqua* satellite. The geophysical data record began on 2 June 2002.

As summarized by Chelton and Wentz (2005), AMSR-E estimates of SST are obtained from measurements of horizontal and vertical polarization at frequencies of 6.9, 10.7, 18.7, 23.8, and 36.5 GHz. Rain-contaminated estimates of SST were identified and excluded from this analysis based on measurements at 36.5 GHz. The accuracy of individual AMSR-E measurements of SST data is about 0.4°C with a footprint size of about 56 km (Chelton and Wentz 2005). As a result of antenna sidelobe contamination at 6.9 GHz, AMSR-E measurements cannot be obtained closer than about 75 km to land. For the analysis in section 3, the downwind and crosswind components of the SST gradient field were computed within each QuikSCAT measurement swath from the nearest 3-day average AMSR-E SST field and the smoothed in-swath QuikSCAT wind stress measurements described in section 2a for the June 2002 through August 2007 period of the AMSR-E data record. The swath-by-swath downwind and crosswind SST gradients were averaged into the same monthly  $0.25^\circ$  latitude  $\times$   $0.25^\circ$  longitude bins as the QuikSCAT wind fields. The seasonal cycles of these SST gradient component time series were computed as described in section 2d in the same manner as the QuikSCAT wind stress fields, except over a 33-

month shorter time period because of the shorter AMSR-E data record.

#### c. NCEP–NCAR reanalysis

The NCEP–NCAR reanalysis project, described in detail in Kalnay et al. (1996) and Kistler et al. (2001), uses an analysis/forecast system to perform assimilation of past data from 1948 to the present. The reanalysis system includes the NCEP global spectral model, with 28 “sigma” vertical levels and a horizontal triangular truncation of 62 spherical harmonics, equivalent to a grid resolution of about 210 km. The dynamical model and data assimilation system are kept unchanged over the reanalysis period. This avoids perceived climate jumps associated with changes in the operational data assimilation system, although it is still affected by changes in the observing systems, particularly by the advent of satellite observations (Kistler et al. 2001). Assimilated data include land surface, ship, rawinsonde, aircraft, and satellite observations. Four-dimensional gridded model fields for more than 30 variables are archived at a 4-times daily temporal resolution as well as daily and monthly composites. The NCEP–NCAR reanalysis grid presently has a zonally uniform spacing of  $1.875^\circ$  and a meridionally nonuniform spacing that varies from  $1.89^\circ$  at the poles to  $2.1^\circ$  near the equator. For this study, monthly composites of the meridional and zonal components of wind stress were analyzed for the 60-yr period January 1948 through August 2007. Monthly wind stress curl and divergence fields were calculated from wind stress fields for the same 60-yr period.

#### d. Harmonic analysis

Previously published wind climatologies, such as HR, COADS, and NOC, which are based on relatively long data records, were computed using a simple arithmetic averaging technique to determine the long-term average for each of the 12 calendar months of the year. In contrast, SCOW is based on harmonic analysis. It is shown in appendix B that the arithmetic averaging method and harmonic analysis generally yield very similar results. Harmonic analysis is preferable for two primary reasons. First, because SCOW is constructed from only 8 yr of data, a highly anomalous month can have undue influence on a simple arithmetic average, thus resulting in a noisy climatology. Harmonic analysis mitigates these effects when constructing a climatology from a shorter data record by effectively utilizing nearby monthly means to reduce the spurious effect of an anomalous individual monthly average. An example is shown in appendix C. Second, the coefficients from harmonic analysis allow the calculation of a climato-

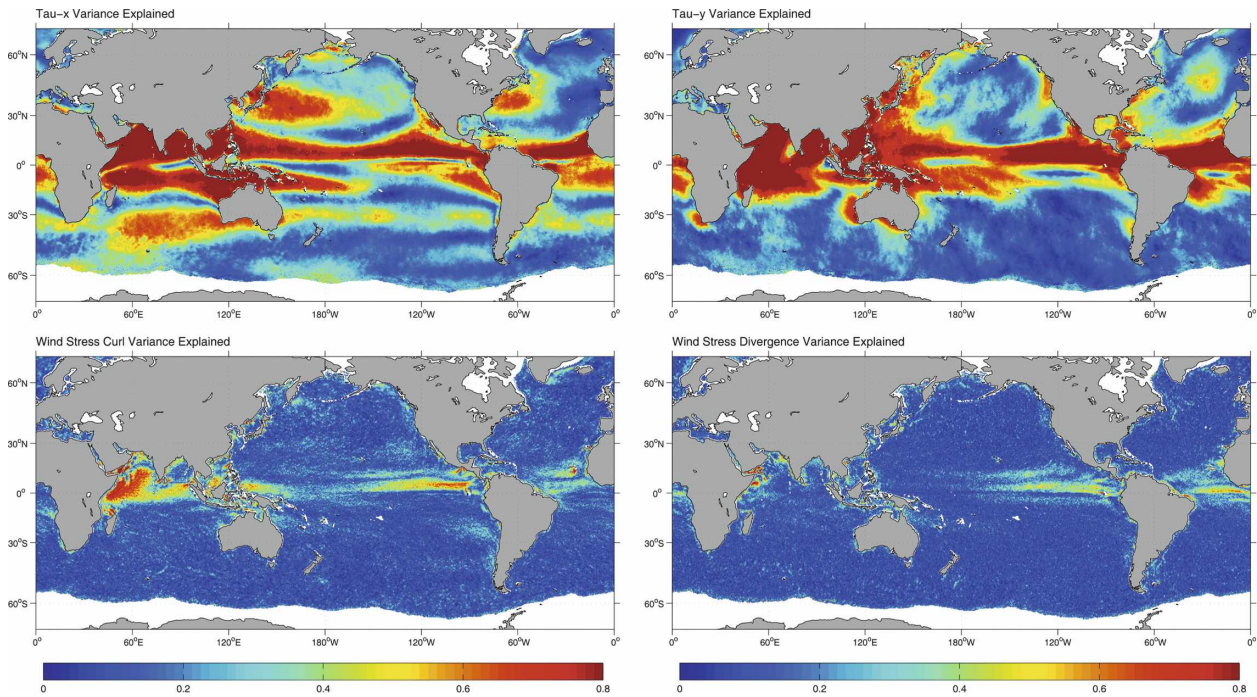


FIG. 3. The fraction of variance explained for (a) zonal and (b) meridional wind stress components for the nine-parameter regression model discussed in section 2d; the fraction of variance explained for (c) wind stress curl and (d) wind stress divergence for the same nine-parameter regression model.

logical value at any arbitrary time. Wind climatologies based on monthly averages require some sort of interpolation scheme to obtain the climatological value at anything other than the monthly intervals at which the climatology was computed. Ocean models require wind forcing at small time increments. A climatology produced by harmonic analysis is therefore far more convenient for modelers than a climatology produced by long-term averaging. The details of our harmonic analysis are described in this section.

The seasonal cycles at each  $0.25^\circ \times 0.25^\circ$  grid point were obtained using the same procedure applied to all of the variables of interest, including those of the SCOW climatology that are listed at the end of section 1 but are not specifically addressed in this study. Each multiyear time series of monthly means was fitted to a nine-parameter regression model consisting of a constant plus four harmonics. This linear regression model can be written as

$$y(t_n) = \hat{y}(t_n) + \hat{\epsilon}(t_n),$$

$$\hat{y}(t_n) = \sum_{m=0}^M \hat{\beta}_m x_m(t_n),$$

where  $\hat{y}(t_n)$  is the regression estimate at time  $t_n$ ,  $M = 8$ ,  $\hat{\beta}_0$  is a constant parameter,  $x_0(t_n) = 1$  for all observation times  $t_n$ , and

$$x_m(t_n) = \begin{cases} \sin(2\pi m f_0 t_n), & m = 1, 3, 5, 7 \\ \cos[2\pi(m - 1)f_0 t_n], & m = 2, 4, 6, 8. \end{cases}$$

The fundamental frequency  $f_0$  is the annual cycle (1 cycle per 12 months). By minimizing the sample mean square of the errors,  $\hat{\epsilon}(t_n)$ , the regression coefficients  $\hat{\beta}_m$  were estimated from the observations  $y(t_n)$  and the trigonometric functions  $x_m(t_n)$ ,  $m = 1, \dots, M$  at  $N = 96$  monthly times  $t_n$ ,  $n = 0, 1, \dots, N - 1$ .

The regression coefficients  $\hat{\beta}_m$  on the  $0.25^\circ \times 0.25^\circ$  grid were spatially smoothed a small amount using a loess smoother (Schlax et al. 2001) with filter cutoff wavelengths of  $1^\circ$  latitude by  $1^\circ$  longitude, analogous to  $0.6^\circ$  block averaging, except that the side lobes of the loess smoother have smaller amplitudes than those of block averages. The seasonal cycle can then be calculated from the smoothed regression coefficients for each  $0.25^\circ \times 0.25^\circ$  grid point using up to four harmonics. From these seasonal cycles, 12 monthly global maps, January through December, of wind stress, wind stress curl, wind stress divergence, and the downwind and crosswind components of the SST gradients were produced for the analyses presented in section 3.

The variances explained for the zonal and meridional wind stress components, as well as the wind stress curl and divergence, are shown in Fig. 3 based on the full

nine-parameter regression model described above. The fraction of variance explained for the zonal and meridional wind stress components (Fig. 3, top left and right, respectively) is relatively low, less than 0.3, over extratropical and high-latitude regions such as the Pacific Ocean sector of the Southern Ocean and the North Pacific and North Atlantic Oceans. The fraction of variance explained for zonal wind stress components is higher in these regions relative to meridional wind stress components, resulting from the fact that winds at high latitudes tend to blow zonally from west to east, strengthening during winter and weakening during summer. In contrast, meridional wind stress components show relatively high temporal variability, associated with the passing of midlatitude cyclones, throughout the year. Seasonal variations are consequently better defined in the zonal component than in the meridional component.

In equatorial regions and off the coasts of North America, South Africa, Chile, and Australia, where winds have relatively strong seasonal cycles, the fraction of variance explained increases to more than 0.6. The same is true of the central and western Pacific, the equatorial Atlantic Ocean, and the Indian Ocean sector of the Southern Ocean.

While the fraction of variance explained by the regression model for wind stress curl (Fig. 3, bottom left) is relatively low over much of the ocean, reflecting the fact that there is much year-to-year variability in the wind stress curl field, it does exceed 0.5 in the east equatorial Pacific Ocean, the North Indian Ocean, and the equatorial Atlantic Ocean, as well as the regions off the west coast of Central America and northern Madagascar and close to island chains such as the Canary Islands.

For wind stress divergence (Fig. 3, bottom right), the fraction of variance explained exceeds 0.5 over the California Current, off the coasts of Somalia, Central America, and northern Madagascar, as well as in the eastern equatorial Pacific and equatorial Atlantic Oceans. Elsewhere, the wind stress divergence field is dominated by year-to-year variability.

It should be noted that the small percentages of variance explained by the seasonal cycles are not attributable to problems with the QuikSCAT data. Rather, the global wind field is dominated by year-to-year variability in most regions. (This is clear from the year-to-year scatter of the monthly means over the 8-yr data record in the example time series in Fig. C1 of appendix C.)

Only the first five coefficients (constant plus annual and semiannual harmonics) were used to construct the seasonal cycles presented in section 3 because of concerns that including higher-order harmonics (three and

four cycles per year) may constitute an overfitting of the seasonal cycle in some regions. These higher-order harmonics, for the most part, account for less than 10% of the variability observed in the wind stress and wind stress derivative fields (not shown). (Note that all nine regressions coefficients are available for download at <http://cioss.coas.oregonstate.edu/scow/>.) Applying these coefficients and the example code provided on the Web page, users can construct seasonal cycles of up to four harmonics, with a temporal resolution that best suits their specific needs (e.g., the short integration time step used in numerical ocean circulation models).

For the analyses in sections 3a,b, the NCEP–NCAR monthly composites of wind stress, wind stress curl, and wind stress divergence described in section 2c were partitioned into two time periods, one spanning the full record length (January 1948–August 2007, hereafter NCEP48) and one that covers the same 8-yr time span as that of the QuikSCAT dataset (September 1999–August 2007, hereafter NCEP99). The seasonal cycles for each NCEP48 and NCEP99 grid point were obtained using the linear regression methodology described above. From these seasonal cycles, monthly global maps, January through December, of wind stress and the wind stress derivative fields were produced. These NCEP–NCAR wind fields were bilinearly interpolated to the QuikSCAT/AMSR-E  $0.25^\circ \times 0.25^\circ$  grid for purposes of comparison in sections 3a,b.

#### e. Accuracy considerations

Although not as difficult as it would be for a ship-based wind stress climatology, it is nonetheless difficult to quantify the accuracy of the QuikSCAT-based SCOW climatological seasonal cycles. Because SCOW was constructed from monthly averaged fields, the first-order question is the accuracy of these monthly averages. The effects of measurement and sampling errors in scatterometer-based spatially and temporally smoothed wind fields have been investigated by Schlax et al. (2001; hereafter SCF01). They show that the accuracy of spatially and temporally smoothed wind fields is much more sensitive to the degree of temporal smoothing than to the degree of spatial smoothing applied to construct wind fields. Because of the complicated space–time sampling pattern of scatterometers (Figs. 6, 8 of SCF01), as well as spatial variability of the variance of wind component fields themselves (Fig. 11 of SCF01), the error fields for small temporal smoothing of the QuikSCAT data can be quite complex (Figs. 12–15 of SCF01), varying spatially at a particular time and temporally at a particular location. The monthly averaged QuikSCAT data used to compute the SCOW seasonal cycles were smoothed in swath with a 70-km

filter half-power point as described in section 2a. This spatial smoothing is close to the minimum  $1^\circ \times 1^\circ$  spatial smoothing considered in Fig. 16 of SCF01. The maximum temporal smoothing considered by SCF01 was 15 days. The monthly averages from which the SCOW climatology was computed correspond to temporally smoothing with a filter half-power point of about 50 days. This is far off the top of the mean and standard deviation error plots in Fig. 16 of SCF01. It is clear from those plots, however, that the errors will be very small for 50-day temporal smoothing.

We believe that any residual effects of measurement and sampling errors in the monthly means from which the SCOW climatology was estimated are less of a concern than the representativeness errors from the 8-yr limitation of the QuikSCAT dataset. The latter is thus likely the largest source of error in the SCOW climatology. The effects of spurious monthly mean values from anomalous geophysical conditions during any particular month and year in the 8-yr data record have been mitigated as summarized in section 2d and appendix C by defining the seasonal cycles by harmonic analysis rather than the more traditional long-term averaging method. Whatever residual errors that might exist in the SCOW climatology are largely offset by the unsurpassed coverage of the QuikSCAT observational dataset, which is the only truly global dataset of highly accurate and frequently sampled high-resolution winds that is available.

Another source of potential error in the QuikSCAT wind fields is the aliasing of diurnal variability that is not fully resolved in the observations at a given location. Gille et al. (2005) have shown that diurnal variability is restricted to coastal and tradewind regions. QuikSCAT samples a given location about twice per day at midlatitudes, with more frequent sampling at latitudes higher than about  $50^\circ$  where measurement swaths from successive orbits overlap, and somewhat less frequent sampling on average at low latitudes where the satellite ground tracks are more widely spaced. The complicated geographical variability of the sampling rate is shown in Figs. 6, 8 of SCF01. The twice-daily samples typical of midlatitudes (one from an ascending orbit and one from a descending orbit) are separated by approximately 12 h, thus barely resolving the  $1 \text{ cycle day}^{-1}$  frequency. Any higher harmonics of this fundamental diurnal cycle will be aliased. Aliasing of even the fundamental diurnal frequency can be problematic at low latitudes where QuikSCAT sampling can be less than twice per day. These aliasing effects are mitigated to some extent by the monthly averaging and harmonic analysis applied to estimate the seasonal

cycles. Quantifying the net effects of aliasing on the SCOW climatology is therefore very difficult.

Because of the much more complete coverage and high spatial resolution of the QuikSCAT observations, the errors in the SCOW climatology are likely smaller than those of any other wind climatology, even with the limitations of the 8-yr duration of the QuikSCAT dataset and potential aliasing of diurnal variability. Representativeness errors from this 8-yr database can be addressed in the future by incorporating additional observations from QuikSCAT and other scatterometers as they become available.

### 3. Results and discussion

#### a. Wind stress fields

The January and July wind stress maps are shown in Fig. 4 for SCOW (top), NCEP99 (middle), and NCEP48 (bottom). The major features known to exist in the wind stress field are all readily visible, including the subtropical anticyclonic gyres in the North and South Pacific, Atlantic, and Indian Oceans, the intertropical convergence zone (ITCZ), year-round strong westerly winds over the Southern Ocean that exceed  $0.25 \text{ N m}^{-2}$  in July, summertime favorable upwelling winds along western continental margins, and strong southwesterly wind stress associated with the South Asian monsoon that exceeds  $0.30 \text{ N m}^{-2}$  off the Somali coast in July and switches to northeasterly with decreased magnitude of about  $0.05 \text{ N m}^{-2}$  in January.

While the SCOW, NCEP99, and NCEP48 January and July fields shown in Fig. 4 are broadly similar with regard to the abovementioned features, significant differences are evident in particular regions. These differences are observable in the top of Fig. 5, which shows the vector difference maps for January and July for SCOW minus NCEP99. SCOW wind stress magnitudes are stronger in the equatorial regions and weaker in regions poleward of about  $35^\circ$  relative to NCEP99. In July in the eastern tropical Pacific Ocean, SCOW wind stress magnitude is about  $0.04 \text{ N m}^{-2}$  stronger than NCEP99. This is consistent with the conclusions of Milliff et al. (1999), who found that NCEP–NCAR wind stress fields are biased low near the equator. This equatorial bias in the NCEP–NCAR wind stress fields has also been noted from comparisons with the ship-based NOC climatology by Josey et al. (2002).

South of  $40^\circ\text{S}$ , NCEP99 wind stress magnitude is typically about 35% stronger than SCOW, with the greatest differences occurring in the Indian Ocean sector of the Southern Ocean. This is consistent with the findings of Josey et al. (2002) who noted, with the ca-

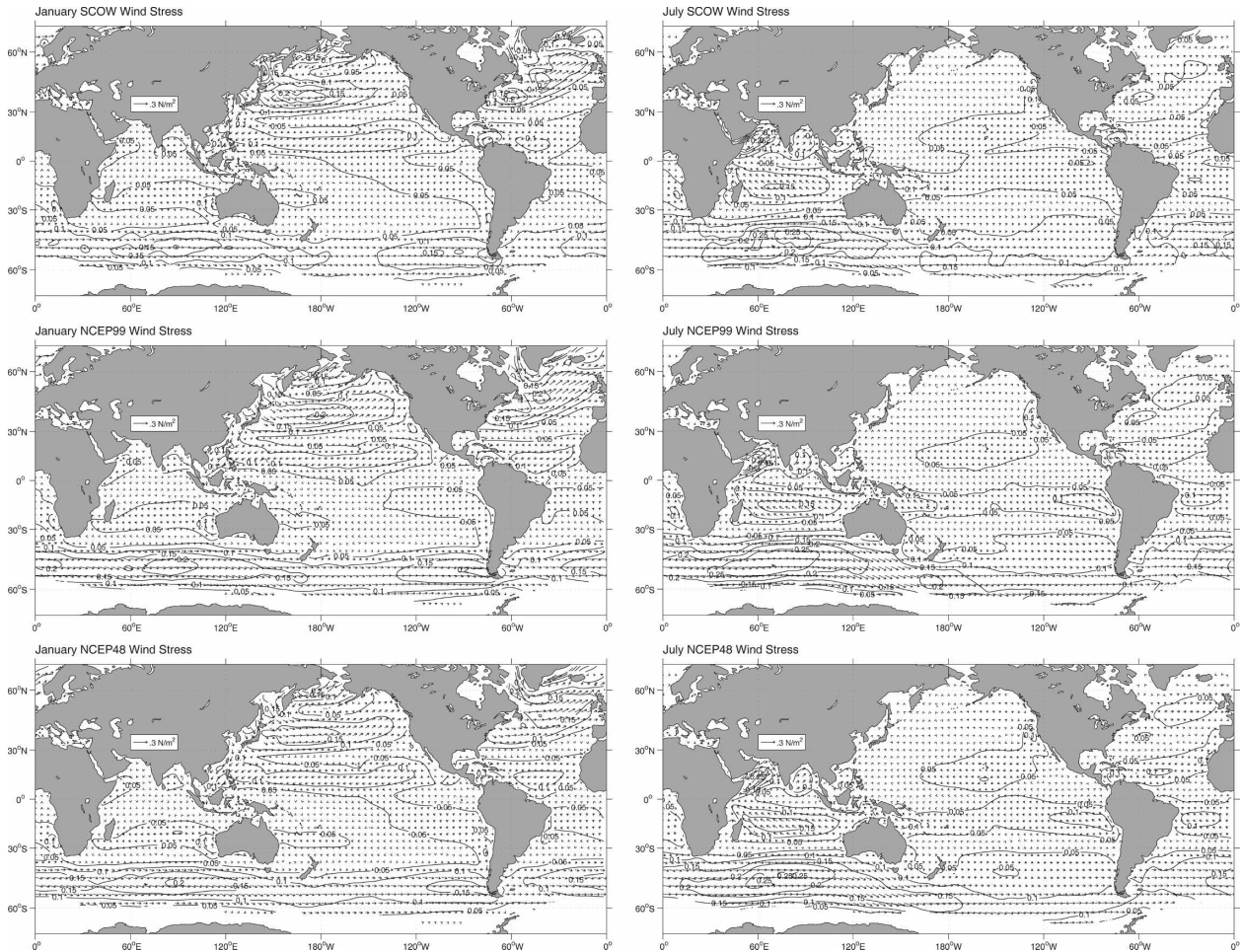


FIG. 4. (a) SCOW January and (b) July wind stress fields. (c), (d) The January and (e), (f) July wind stress fields are shown for NCEP99 and NCEP48. For the purpose of comparison, the NCEP–NCAR fields are interpolated to the SCOW  $0.25^\circ \times 0.25^\circ$  grid. Wind stress vectors are plotted on a coarse  $4^\circ \times 4^\circ$  grid for clarity. Contours of spatially smoothed vector-averaged wind stress magnitude are plotted in all six panels with a contour interval of  $0.05 \text{ N m}^{-2}$ .

veat that there are very few in situ ship observations in this region, that the NOC wind stress magnitude is about 40% weaker than annual mean ECMWF and NCEP–NCAR reanalysis wind stress fields between  $50^\circ$  and  $55^\circ\text{S}$ . An interesting exception to the general finding that NCEP99 wind stress magnitude tends to be stronger than that of SCOW south of  $40^\circ\text{S}$  is the region of the South Indian Ocean between  $40^\circ$  and  $45^\circ\text{S}$  and  $25^\circ$  and  $70^\circ\text{E}$  where SCOW wind stress magnitudes are stronger than NCEP99. This region of locally increased wind stress magnitude is most visible in July and is attributable to air–sea interaction over the meandering Agulhas Return Current, which results in locally intensified wind stress over warm water and decreased wind stress over cold water (O’Neill et al. 2003, 2005). This well-documented phenomenon, discussed in greater detail in sections 3b,d, is poorly resolved in the coarse-

resolution NCEP–NCAR reanalysis fields (see Figs. 6, 8). There is little to no evidence of these air–sea interactions in the HR, NOC, and TLO climatologies.

Other notable differences between SCOW and NCEP99 exist in regions close to the Hawaiian Islands, off Central America, and south of Greenland, arising from corner accelerations and gap wind features that are poorly resolved in the NCEP–NCAR reanalysis wind fields. These phenomena can be important to ocean and atmosphere dynamics. Pickart et al. (2003), for example, suggest that the Greenland corner acceleration is an important precursor to localized deep ocean convection in the southern Irminger Sea, providing an additional source of the so-called Labrador Sea Water. The effects of the Hawaiian Islands are discussed by Xie et al. (2001) and the effects of Central American gap winds on the Pacific ocean–atmosphere

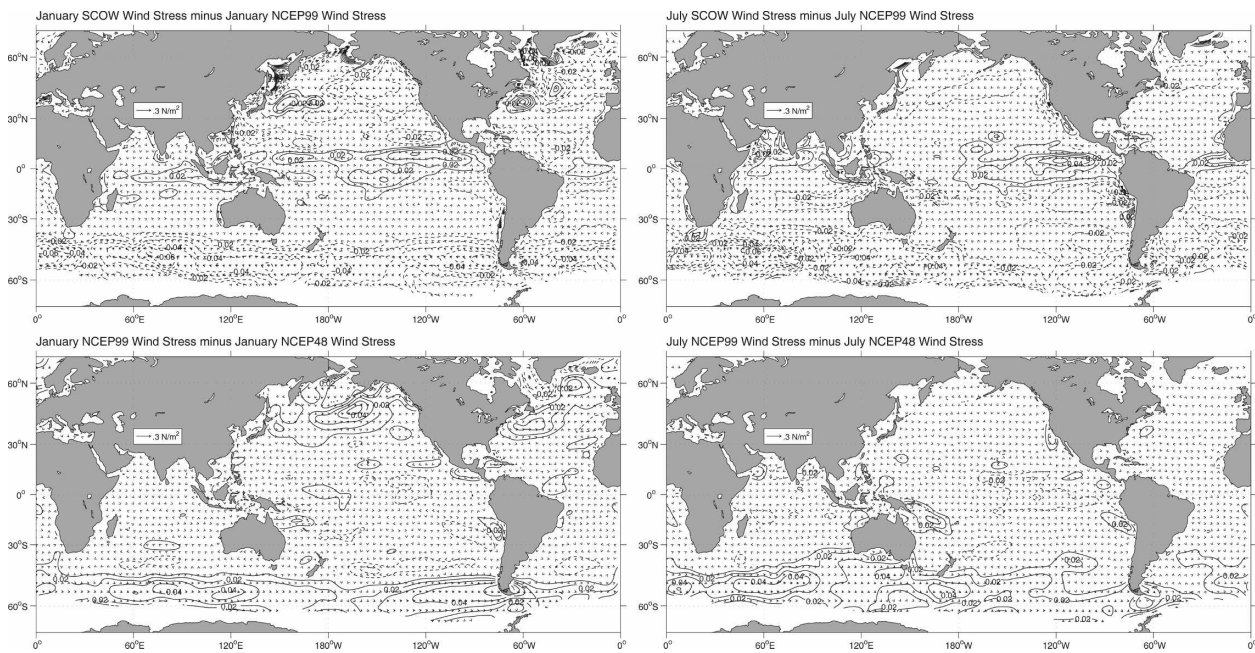


FIG. 5. The wind stress vector difference for (a) January and (b) July for SCOW minus NCEP99. (c), (d) The same for NCEP99 – NCEP48. Differenced wind stress vectors are plotted on a coarse  $4^\circ \times 4^\circ$  grid for clarity. Contours of differenced, spatially smoothed vector-averaged wind stress magnitude are plotted in all four panels with a contour interval of  $0.01 \text{ N m}^{-2}$ . The zero contour is omitted for clarity, and negative contours are dashed.

system are discussed by Chelton et al. (2000a,b), Bourassa et al. (1999), and Xie et al. (2005).

The bottom of Fig. 5 shows the differences between NCEP99 and the long-term 60-yr NCEP48 wind stress climatology. The largest differences are found in high-latitude regions. In the Indian and Pacific sectors of the Southern Ocean, south of  $40^\circ\text{S}$ , NCEP99 wind stress magnitude is between 20% and 35% stronger than NCEP48. The strengthening of wind stress over the Southern Ocean is consistent with the findings of Huang et al. (2006), who showed from 56 yr of daily averaged NCEP–NCAR reanalysis wind stress fields that there has been a 12% increase in energy input from wind stress over the 25-yr period 1979 through 2003. The bulk of this global estimate results from an increase in wind stress over the Southern Ocean. Between  $40^\circ$  and  $60^\circ\text{S}$ , the decadal mean zonal wind stress increased from about  $0.12 \text{ N m}^{-2}$  between 1950 and 1959 to about  $0.17 \text{ N m}^{-2}$  between 1990 and 1999 (see Fig. 11 of Huang et al. 2006). South of the Aleutian Islands, NCEP99 wind stress magnitude exceeds NCEP48 by about 40% in January. In contrast, NCEP99 wind stress magnitude is about 20% weaker than NCEP48 south of Greenland in January.

It is difficult to say for certain to what degree the differences between NCEP99 and NCEP48 are indicative of interannual variability in the wind field. Steady

improvements in the observational system, especially the satellite observations that are assimilated in the NCEP–NCAR reanalyses, could be responsible for some of the apparent differences in the bottom of Fig. 5. This is particularly the case in high-southern-latitude regions where very little in situ data were available before the satellite era. To the extent that the differences between NCEP99 and NCEP48 are real, care must be exercised in the use of the SCOW climatology because it may not be representative of the long-term seasonal cycle at high latitudes.

### b. Wind stress derivative fields

The nature of the differences between SCOW and NCEP99 become more apparent in the wind stress curl and wind stress divergence fields (shown in Figs. 6, 8, respectively). This is because spatial high-pass filtering of the derivative operations emphasize the small-scale variability that is poorly resolved in the NCEP–NCAR reanalysis wind fields. The global derivative wind stress fields are discussed in this section.

#### 1) WIND STRESS CURL

On large scales, the wind stress curl field over much of the world's oceans is very similar in SCOW and the

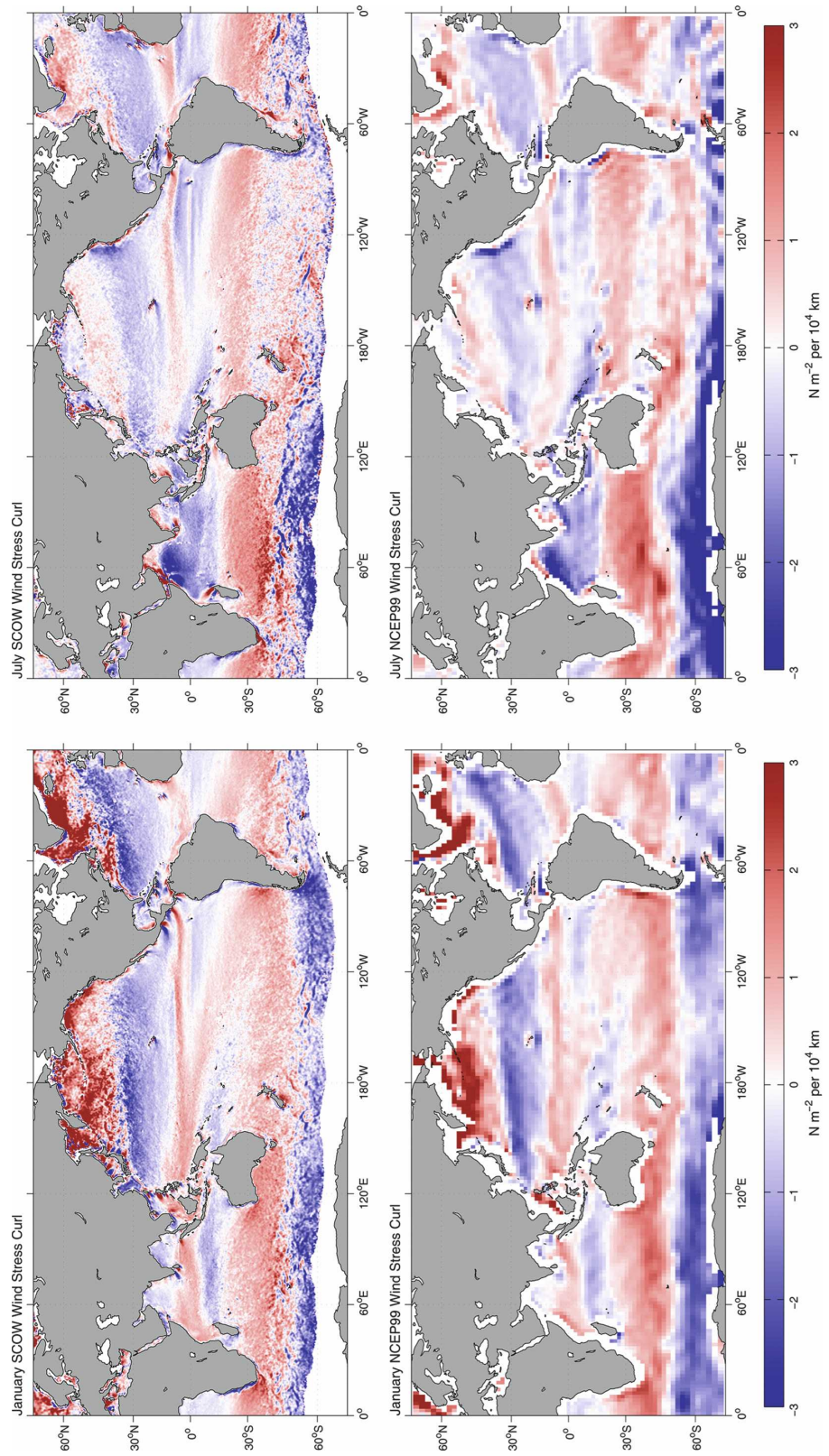


FIG. 6. (top) Global SCOW and (bottom) NCEP99 wind stress curl maps for (left) January and (right) July. The SCOW fields are plotted on a  $0.25^\circ \times 0.25^\circ$  grid. The NCEP99 fields are plotted on a grid that has a zonally uniform spacing of  $1.875^\circ$  and a meridionally nonuniform spacing that varies from  $1.89^\circ$  at the poles to  $2.1^\circ$  near the equator. The wavelike variations that appear throughout the NCEP99 fields are artifacts of spectral truncation of mountain topography in the spherical harmonic NCEP–NCAR reanalysis model (Milliff and Morzel 2001).

NCEP–NCAR reanalysis winds (Fig. 6). In general, meridional shears between easterly trade winds, mid-latitude westerlies, and polar easterlies result in a Northern (Southern) Hemisphere pattern of positive (negative) wind stress curl in subpolar regions and negative (positive) curl in subtropical regions. Along western continental margins, narrow bands of cyclonic curl (positive and negative in the Northern and Southern Hemispheres, respectively) are visible in the SCOW fields but poorly resolved in the NCEP99 fields. These bands of cyclonic curl are oceanographically important as they help drive the upwelling of nutrient-rich waters in these dynamic and economically important eastern boundary current regions.

Many small-scale features that are clearly visible in the SCOW wind stress curl fields are missing from the relatively coarse-resolution NCEP99 wind stress curl fields. These include orographically induced features such as island corner accelerations and wind shadows (Xie et al. 2001, 2005; Chelton et al. 2004), gap winds in Central America (Bourassa et al. 1999; Chelton et al., 2000a,b), between the north and south islands of New Zealand, between the southern tip of India and Sri Lanka, off the northern tip of Madagascar, and the corner accelerations south of Greenland (Doyle and Shapiro 1999; Moore 2003), and north of Columbia. Some of these features, which have previously been noted in the 4-yr average QuikSCAT wind stress curl field presented by Chelton et al. (2004), are detectable, albeit at a coarser resolution, in the NOC July wind stress curl field (bottom right of Fig. A1 in appendix A).

A notable difference between the July SCOW and NCEP99 wind stress curl fields is the latitudinal banding of alternating negative and positive wind stress curl that straddles the equator over about  $50^{\circ}$  of longitude within  $\pm 10^{\circ}$  of the equator to the south of the ITCZ in the eastern Pacific. Similar alternating bands of negative and positive curl have previously been noted from the 9-month-average NSCAT wind stress field presented by Milliff and Morzel (2001) and from the first 4 yr of QuikSCAT data by Chelton et al. (2004). This banding is due to the influence of SST on surface winds (Chelton et al. 2001, 2004; Chelton 2005). The HR and NOC annual average wind stress curl fields presented in Josey et al. (2002) and the annual average TLO wind stress curl field show only broad regions of negative wind stress curl in this region, similar to the NCEP–NCAR reanalyses in Fig. 6. While somewhat ambiguous, the July NOC wind stress curl field (bottom right of Fig. A1 in appendix A) does show evidence of this band of positive curl. These features in SCOW that are poorly resolved by other climatologies emphasize the

benefits of the high spatial resolution of the QuikSCAT data.

The low resolution of the NCEP99 wind stress curl fields is due partly to the coarse grid resolution of the NCEP–NCAR reanalysis model and partly to the low resolution of the Reynolds SST analyses that are used as ocean boundary conditions in the NCEP–NCAR model. In a study that compares ECMWF wind stress fields with QuikSCAT wind stress observations during the August–December cold seasons of 2000 and 2001, Chelton (2005) showed that the use of a higher-spatial-resolution real-time global (RTG) SST boundary condition for the ECMWF model beginning in May 2001 significantly improved the model's ability to resolve wind stress curl perturbations in the eastern Pacific (see also Chelton and Wentz 2005; Maloney and Chelton 2006 for midlatitude examples). If the NCEP–NCAR reanalysis procedure were to utilize a higher-resolution SST boundary condition such as that recently produced by Reynolds et al. (2007), which dates from January 1985 to the present, it could better resolve the narrow zonal bands of alternating positive and negative wind stress curl visible in SCOW in the eastern Pacific, though the present coarse-grid resolution would still limit the impact of SST on the model wind fields.

The influence of SST on the surface wind stress field is evident in Fig. 6 as small-scale structures in the SCOW wind stress curl and divergence fields in regions of strong SST gradients, as discussed extensively by Chelton et al. (2004) and Maloney and Chelton (2006). Regional examples are presented in section 3d. SST gradients influence the marine atmospheric boundary layer (MABL) by modifying its stability through changes in air-sea heat flux. Colder waters act to stabilize the MABL. This inhibits the vertical turbulent mixing of momentum from aloft to the surface and results in a shallowing of the MABL and a deceleration of surface winds. The reverse is true over warmer waters where increased surface heat fluxes destabilize and deepen the MABL. This destabilization enhances the vertical turbulent mixing of momentum from aloft to the surface and results in an acceleration of surface winds. SST-induced perturbations in atmospheric pressure at the sea surface and nonlinear advection also play significant roles in the overall surface wind response to SST (Lindzen and Nigam 1987; Small et al. 2005; Samelson et al. 2006; O'Neill et al. 2008, manuscript submitted to *J. Climate*).

As a consequence of the SST influence on surface winds, a wind stress curl develops over regions of strong crosswind SST gradients (Chelton et al. 2001, 2004). Likewise, a wind stress divergence develops in regions of strong downwind SST gradients. This SST influence

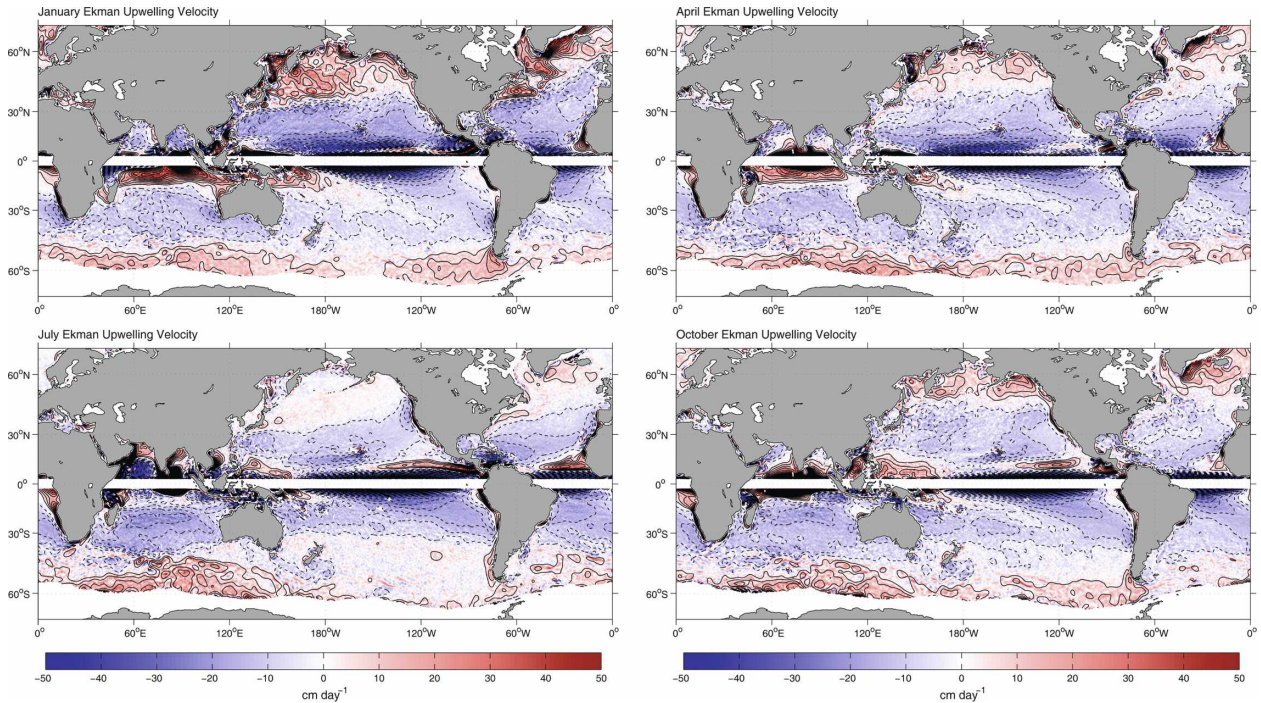


FIG. 7. Average SCOW Ekman upwelling velocity ( $w$ ) maps for (a) January, (b) April, (c) July, and (d) October. Given that  $\text{curl}(\tau/f)$  is undefined at the equator, values of  $w$  are not plotted between  $3^\circ\text{S}$  and  $3^\circ\text{N}$ . Contours of  $w$  with an interval of  $5 \text{ cm day}^{-1}$  are overlaid to aid interpretation. Dashed and solid contours correspond to negative and positive upwelling velocities, respectively. The zero contour is omitted for clarity.

on the surface wind stress field is poorly represented in global numerical prediction and climate models, including NCEP–NCAR (Fig. 6, bottom), resulting in an overly smooth structure in the global wind fields in these models (Chelton et al. 2004; Chelton and Wentz 2005; Maloney and Chelton 2006).

## 2) EKMAN PUMPING

The curl of the wind stress generates open ocean upwelling and downwelling, often referred to as Ekman pumping. The Ekman upwelling velocity at the base of the surface Ekman layer is

$$w = \frac{1}{\rho} \text{curl}\left(\frac{\tau}{f}\right) = \frac{1}{\rho f} \text{curl}(\tau) + \frac{\beta}{f^2} \tau_x,$$

where,  $\tau$  is the vector wind stress,  $\tau_x$  is the eastward component,  $f$  is the Coriolis parameter, and  $\rho$  is the water density, assumed to be  $1025 \text{ kg m}^{-3}$ . Figure 7 shows average global distributions of  $w$ , estimated from SCOW wind stress curl fields for January (top left), April (top right), July (bottom left), and October (bottom right). Except near eastern boundaries, upwelling and downwelling regions tend to be zonally oriented. In association with the large-scale wind stress curl patterns, subtropical regions tend to be associated with

downwelling, while the reverse is true of subpolar regions. The Ekman model breaks down close to the equator where  $f$  approaches zero, resulting in very strong upwelling and downwelling. The upwelling estimates in Fig. 7 are probably not valid closer than  $5^\circ$  to the equator.

Seasonal changes in Ekman pumping are clearly evident in the North Pacific and Atlantic Oceans, where upwelling velocities exceed  $20 \text{ cm day}^{-1}$  in January but are reduced to less than  $5 \text{ cm day}^{-1}$  in July. In the North Indian Ocean, intense downwelling associated with the southwest monsoon is observed in July. While not as marked, seasonal changes in the Southern Hemisphere are also observed in Fig. 7. This is particularly true of the South Indian Ocean where downwelling values of approximately  $5$  and  $10 \text{ cm day}^{-1}$  are observed for January and July, respectively.

## 3) WIND STRESS DIVERGENCE

While wind stress divergence has no effect on ocean currents, it is a clear indicator of the ocean–atmosphere interaction discussed above. Figure 8 shows the wind stress divergence fields for January (left) and July (right) for SCOW (top) and NCEP99 (bottom). SCOW shows parallel zonal bands of strong divergence just

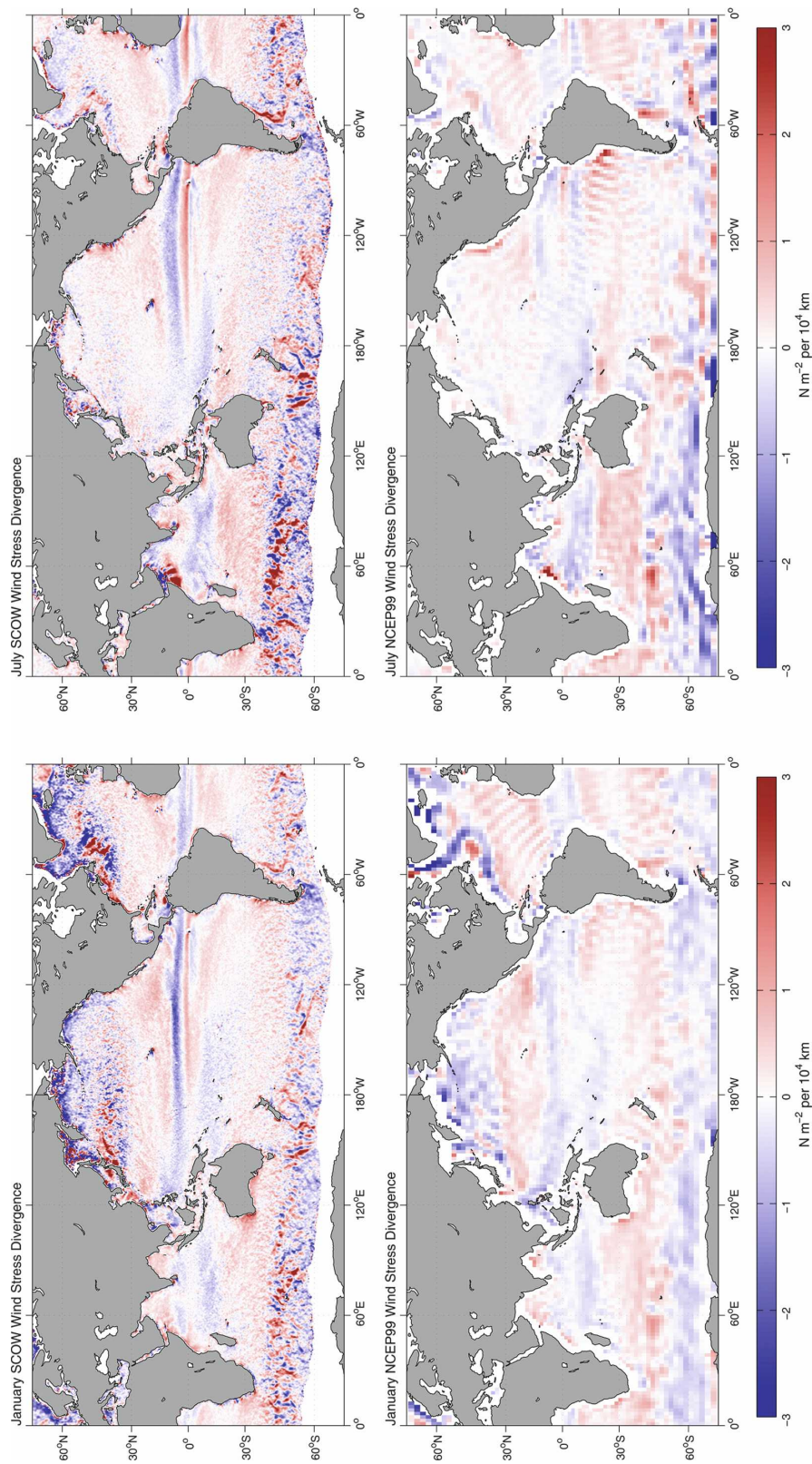


FIG. 8. Same as in Fig. 6, except for wind stress divergence.

north of the equator in the Atlantic and Pacific Oceans. These bands of convergence (negative values) and divergence (positive values) are the result of southeast trade winds decelerating and accelerating, respectively, across the SST fronts on both sides of the equatorial cold tongues (Chelton et al. 2001; Hashizume et al. 2001; Chelton 2005). Air-sea interactions in the eastern tropical Pacific are discussed in greater detail in section 3d(5).

Outside of the tropics, SST influence on surface winds is mostly restricted to regions poleward of 35° latitude. Lower-latitude exceptions are found regionally where winds blow across strong and persistent SST fronts. Off the coast of Namibia, a region that is discussed in greater detail in section 3d(2), the influence of offshore jets of cold water associated with year-round upwelling is clearly observable as alternating convergence and divergence bands. The July SCOW panel of Fig. 8 shows bands of strong positive and negative divergence off the coast of Somalia (Vecchi et al. 2004). These striations are associated with southwest monsoon winds blowing across the SST fronts of two large anticyclonic eddies, the so-called Great Whirl (Schott et al. 1997) and the so-called Southern Gyre (Schott and McCreary 2001), which are associated with the Somali Current. The orographic influence of island chains such as the Hawaiian Islands is visible in the top of Fig. 8. The localized patches of alternating negative and positive divergence between the islands is evidence of the wind shadows behind each island and wind jets accelerating through interisland gaps, respectively. The influence that these features have on the underlying ocean is discussed by Xie et al. (2001).

Poleward of 35°, alternating patches of divergence and convergence are apparent throughout the Southern Ocean and in the northwest Atlantic and Pacific Oceans (Fig. 8, top). The divergence and convergence patterns in the Southern Ocean result from accelerations and decelerations of the mean westerly winds as they blow across meandering SST fronts that are associated with bathymetrically induced stationary meanders of the Antarctic Circumpolar Current (ACC) (O'Neill et al. 2003, 2005). The divergence and convergence patterns visible in the northwest Atlantic result from the acceleration of northwesterly winds over the relatively warm water of the Gulf Stream and the subsequent deceleration over the relatively cool water of the Sargasso Sea. The strong divergence that occurs east of Newfoundland is the result of westerly winds accelerating across the warm Gulf Stream after it turns northward around Grand Banks [see section 3d(1) for a more detailed discussion]. Similar wind stress diver-

gence structure associated with the relatively warm Kuroshio can be seen in the northwest Pacific (Nonaka and Xie 2003).

The most striking features in the NCEP-NCAR reanalysis curl and divergence fields in the bottom of Figs. 6, 8 are the wavelike variations that appear to be radiating outward from South America and western Europe. As discussed previously, these patterns result from the spectral truncation of mountain topography in the spherical harmonic NCEP-NCAR model (Milliff and Morzel 2001).

### c. Sverdrup circulation

The significance of the higher resolution of the SCOW climatology to the large-scale ocean circulation can be assessed from the Sverdrup circulation computed from the 8-yr-average SCOW wind stress curl field. The streamfunction  $\psi_s$  of the volume transport of the Sverdrup circulation was determined by integrating zonally from a boundary value of zero at the eastern margin  $x_0$  of each of the major ocean basins to a given longitude  $x$  according to the following equation (e.g., Pedlosky 1987):

$$\text{psi}_s(x) = \int_{x_0}^x \frac{1}{\rho\beta} (\nabla_H \times \tau) dx' + \psi(x_0),$$

where  $\rho$  is the water density, assumed to be 1025 kg m<sup>-3</sup>,  $\beta = df/dy$  is the latitudinal variation in the Coriolis parameter  $f = 2\Omega \sin\theta$  for earth rotation rate  $\Omega$  and latitude  $\theta$ , and  $\nabla_H = \mathbf{x}\partial/\partial x + \mathbf{y}\partial/\partial y$  for unit vectors  $\mathbf{x}$  and  $\mathbf{y}$  along the  $x$  and  $y$  axes. The so-called island rule was used to calculate  $\psi_I$  around the boundaries of New Zealand and Australia (de Szoeke 1987; Godfrey 1989). The island rule yields an expression for the streamfunction at the island in terms of the integral of the wind stress around a closed path enclosing the island,

$$\psi_I = \frac{1}{\rho(f_s - f_n)} \oint \tau \cdot d\mathbf{s},$$

where  $f_s$  and  $f_n$  are the values of the Coriolis parameter along the southern and northern latitudes of the closed integration path. The closed integration paths are shown in Fig. 15 of de Szoeke (1987). The resulting values for the streamfunction around New Zealand and Australia are used to initiate the integration westward from these islands.

The values of  $\psi_I$  obtained in this study using the 12-month-average SCOW wind stress curl field and the 12-month-average NCEP99 and HR wind fields are listed in Table 1. The corresponding values from de Szoeke (1987) and Godfrey (1989) are also listed in

TABLE 1. The values of the streamfunction for New Zealand ( $\Psi_{\text{NZ}}$ ) and Australia ( $\Psi_{\text{AUS}}$ ) obtained by the island rule based on the 12-month-average SCOW, NCEP99, and HR wind stress curl fields. Also shown are the values of  $\Psi_{\text{NZ}}$  and  $\Psi_{\text{AUS}}$  obtained from the 12-month-average HR wind stress curl field by de Szoeke (1987) and Godfrey (1989).

	$\Psi_{\text{NZ}}$	$\Psi_{\text{AUS}}$
SCOW	-25	-14
NCEP99	-35	-15
HR	-28	-18
de Szoeke (1987)	-29	-17
Godfrey (1989)	-29	-16

Table 1 for purposes of comparison. While there is little difference between the SCOW and NCEP99 streamfunction values for Australia, the SCOW streamfunction value for New Zealand is 44% smaller than that from NCEP99. This is largely because NCEP99 wind stress magnitudes tend to be stronger in regions poleward of about 40°S relative to SCOW.

The Sverdrup transport streamfunction  $\psi_s$  computed from the 12-month-average SCOW and NCEP99 wind stress curl fields is shown in Fig. 9 (top and middle respectively). The differences between the two estimates of the Sverdrup circulation are contoured in the bottom of Fig. 9. The arrows on all three panels indicate the direction of the volume transport. The largest differences occur in the Southern Ocean and in the western tropical Pacific in association with the latitudes of largest differences between the SCOW and NCEP99 wind stress curl fields discussed in section 3b(1).

Latitudinal profiles of the Sverdrup volume transport values along the western boundaries are shown in Fig. 10 for SCOW, NCEP99, and NOC for the Pacific (top left) and Atlantic Oceans (top right). The differences are plotted in the bottom left and right panels. The differences between NCEP99 and SCOW as well as between NOC and SCOW transport values along the western boundaries of the Pacific and Atlantic Oceans are mostly less than 10 Sv (1 Sv  $\equiv 10^6 \text{ m}^3 \text{ s}^{-1}$ ). Large differences, however, are observed in the Pacific Ocean approximately 10° north and south of the equator and in the ACC. In the northwestern tropical Pacific (~12°N) NCEP99 (~38 Sv) and NOC (~29 Sv) transport values exceed SCOW (~15 Sv) by about 153% and 93%, respectively. In the southwestern tropical Pacific (~10°S) the percent differences are even larger with NCEP99 (~22 Sv) and NOC (~15 Sv) transport values exceeding SCOW (~4 Sv) by about 450% and 275%, respectively. Between 35° and 45°S, SCOW transport values exceed NOC by as much as 80 Sv. Poleward of 45°S, NCEP99 transport values exceed SCOW by up to about 60 Sv.

#### d. Regional studies

There are many interesting features in the SCOW wind stress fields presented above that are difficult to discern in detail in the global maps in Figs. 4, 6, 8 and may be surprising to the uninitiated reader. We therefore summarize in this section some regional examples that illustrate the variety of phenomena that can explain these features based on previously published analyses. We do not intend for this to be a rigorous or comprehensive analysis. Ample references are provided for the reader to find the necessary rigor in the literature.

Figures 11–15 show SCOW wind stress, wind stress curl, and stress divergence fields for five regions for months that are most interesting for each particular region. These regions are highlighted here for three reasons. First, associated with all five regions are strong SST fronts that have a profound influence on surface ocean winds. Second, regions such as the California Current and Benguela Current systems are noteworthy because of their direct economic importance, through fishing, to countries such as the United States, Mexico, South Africa, and Namibia. Lastly, the eastern tropical Pacific Ocean is highlighted because of its connection to El Niño Southern Oscillation (ENSO) and because it contains a number of interesting and dynamically important wind features.

#### 1) NORTHWEST ATLANTIC OCEAN

The northwest Atlantic Ocean is the subject of some of the earliest investigations of the effect of SST gradients on the low-level wind stress field. Using aircraft surveys across the Gulf Stream, Sweet et al. (1981) showed that winds are generally stronger over the warm side of the Gulf Stream than over the cold side. More recently, Chelton et al. (2006), using observations from a QuikSCAT overpass on 16 February 2005, show an example of wind speeds of 10–14 m s<sup>-1</sup> on the warm (south) side of the North Wall of the Gulf Stream, defined to be the 17.5°C SST isotherm, and 4–7 m s<sup>-1</sup> wind speeds on the cold (north) side of the North Wall. Park et al. (2006) show modification of scatterometer-derived wind fields by currents and SST gradients near frontal boundaries of Gulf Stream rings, and Song et al. (2006) and Minobe et al. (2008) have investigated the SST influence on surface and tropospheric winds over the Gulf Stream itself.

Perhaps surprisingly, evidence of similar air-sea interaction is visible in the SCOW climatological wind stress and wind stress derivative fields, indicating that these are seasonally recurring features. The left panel

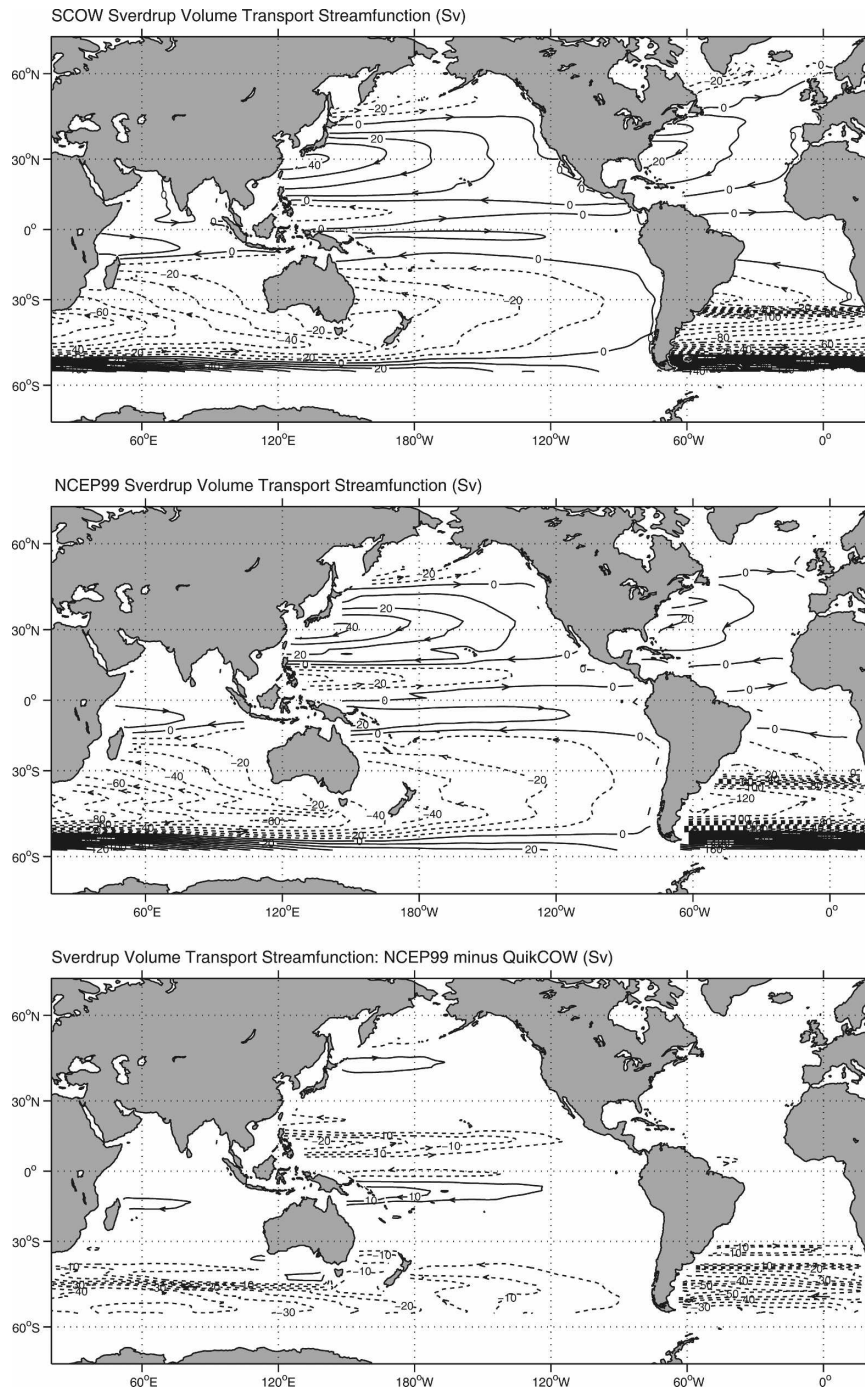


FIG. 9. Sverdrup volume transport streamfunction (Sv) computed from the 12-month-average (a) SCOW and (b) NCEP99 wind stress curl fields. (c) The differences between the two estimates of the Sverdrup circulation are contoured. The contour interval for the top and middle panels is 10 Sv. The contour interval for the bottom panel is 5 Sv, and the zero contour is omitted for clarity. Negative contours are dashed in all three panels.

of Fig. 11 shows January vector-averaged wind stress magnitude depicted in color. Overlaid are vectors that show vector-averaged wind stress direction. Two broad regions of relatively strong wind stress, one centered at

39°N, 61°W and one centered at 48°N, 43°W, are evident. The middle panel of Fig. 11 shows the January wind stress curl field in color with contours of ASMR-E crosswind SST gradients overlaid. Positive (negative)

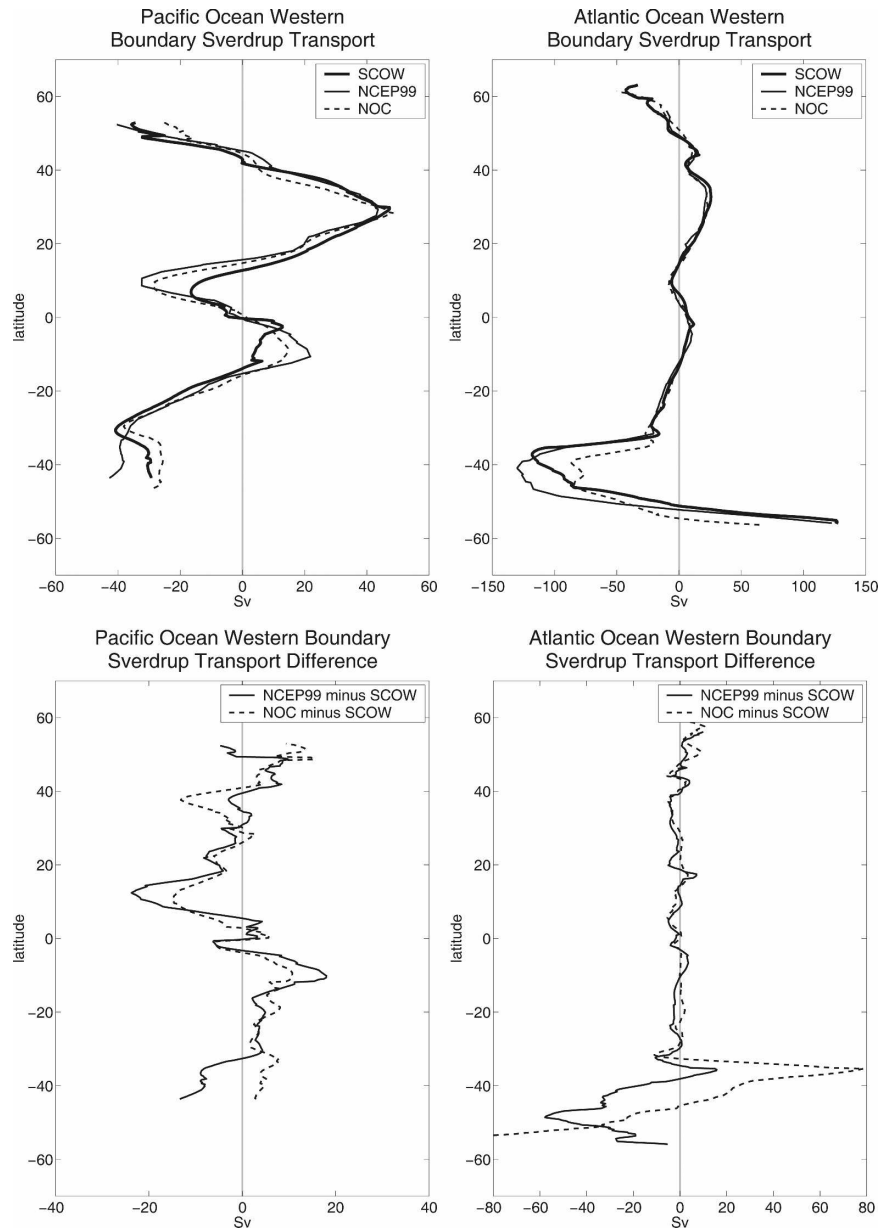


FIG. 10. SCOW (heavy solid line), NCEP99 (thin solid line), and NOC (dashed line) western boundary Sverdrup volume transport values for the (a) Pacific and (b) Atlantic Oceans. The differences between SCOW and NCEP99 (thin solid line) and SCOW and NOC (dashed line) for the (c) Pacific and (d) Atlantic Oceans are plotted. Note the changes in the dynamic range of the  $x$  axis for all four panels.

wind stress curl is collocated with positive (negative) crosswind SST gradients.

Along the east coast of the United States, south of Cape Hatteras, a couplet of parallel bands of positive and negative wind stress curl straddles the Gulf Stream. This feature results from the fact that scatterometers measure the actual stress imposed on the sea surface by the wind. This stress depends on the difference between wind and ocean velocities. As a result, significant modi-

fication of the wind stress field occurs in regions of strong currents (Cornillon and Park 2001; Kelly et al. 2001; Chelton et al. 2004). When viewed in the direction of flow, the Gulf Stream is manifest as parallel bands of negative and positive curl straddling the left and right sides of the current, respectively. A similar feature is clearly visible in the 4-yr-average QuikSCAT wind stress curl field presented in Chelton et al. (2004).

On the scales of interest here, ocean velocity is quasi-

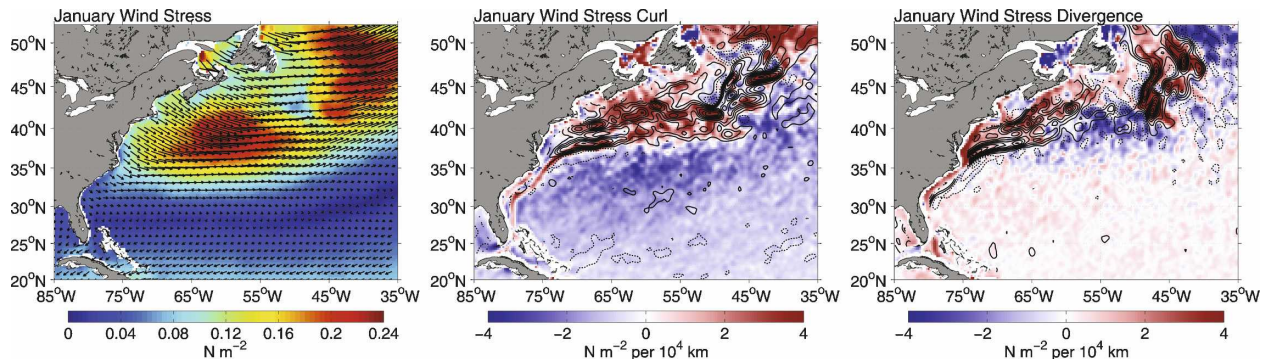


FIG. 11. January maps of wind stress and wind stress derivatives over the northwest Atlantic Ocean. (left) Vector-averaged wind stress magnitude in color with vectors overlaid to depict vector-averaged wind stress direction. Every fourth wind stress vector is plotted for clarity. (middle) Wind stress curl and (right) divergence fields for January with contours of ASMR-E crosswind and downwind SST gradients overlaid at an interval of  $0.4^{\circ}\text{C}$  ( $100 \text{ km}$ ) $^{-1}$ , respectively. Dashed and solid contours correspond to negative and positive SST gradients, respectively. The zero contour is omitted for clarity.

geostrophic and very nearly nondivergent. Consequently, while the effects of ocean currents on surface wind stress are readily apparent in the curl field, they are inconsequential in the divergence field. The bands of divergence and convergence associated with the Gulf Stream in the right panel of Fig. 11 are associated with the previously discussed effect of SST on surface wind stress. East of Newfoundland is a region of strong positive divergence that results from westerly winds accelerating from cold to warm water across the Gulf Stream after it turns northward around the Grand Banks. This region of strong divergence is collocated with positive downwind temperature gradients.

## 2) BRAZIL–MALVINAS CONFLUENCE

The Brazil Current is the western boundary current for the South Atlantic subtropical gyre. This relatively weak current (Peterson and Stramma 1991) carries warm subtropical water poleward along the continental

margin of South America to about  $33^{\circ}$ – $38^{\circ}\text{S}$  (Olson et al. 1988), where it encounters the Malvinas Current that transports cold freshwater equatorward along the South American continental shelf. The confluence of the Brazil and Malvinas Currents results in a region of strong SST fronts (Goni et al. 1996), which are oriented meridionally west of  $52^{\circ}\text{W}$  (Garzoli 1993; Legeckis and Gordon 1982). In addition, a strong eastward jet associated with the ACC forms a zonal SST front along  $49^{\circ}\text{S}$  (Niiler et al. 2003).

Westerly wind stress prevails over the Brazil–Malvinas Confluence in July (left of Fig. 12). South of Cape Horn and northwest of the Malvinas/Falkland Islands, wind stress magnitudes of about  $0.14 \text{ N m}^{-2}$  are observed. North of the Malvinas/Falkland Islands is a region of strong positive wind stress curl and divergence (Fig. 12, middle and right, respectively). East-northeast of the Malvinas/Falkland Islands is a zonal band of negative wind stress curl that is associated with the aforementioned ACC frontal zone. The former and

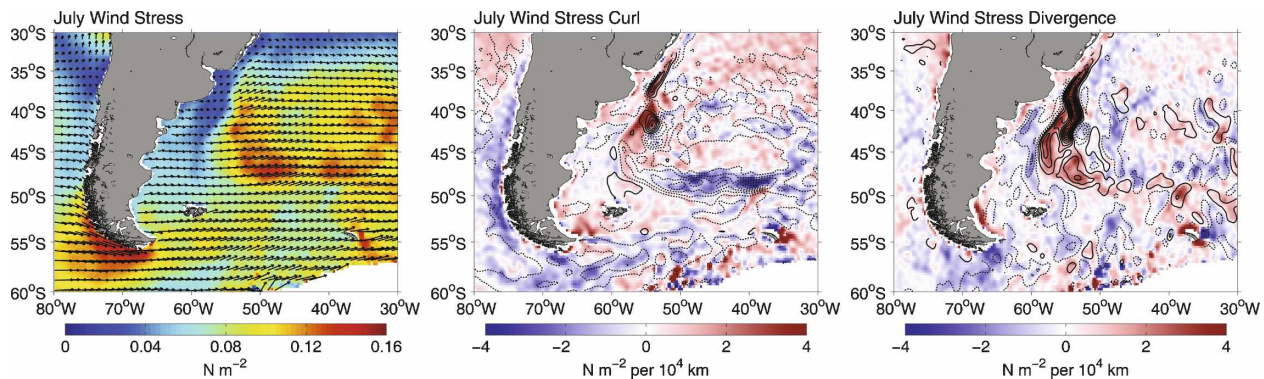


FIG. 12. Same as in Fig. 11, except for the Brazil–Malvinas Confluence for July. Note the change in dynamic range for wind stress magnitude.

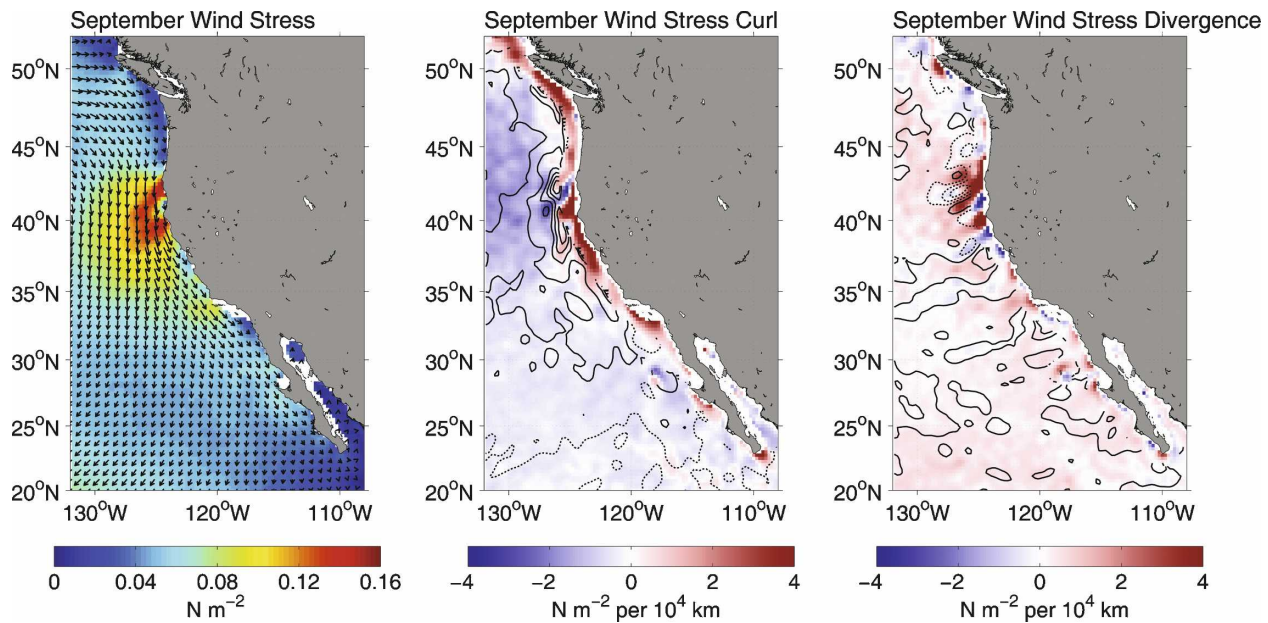


FIG. 13. Same as in Fig. 11, except for the CCS for September. Every third wind stress vector is plotted for clarity. Note the change in dynamic range for wind stress magnitude.

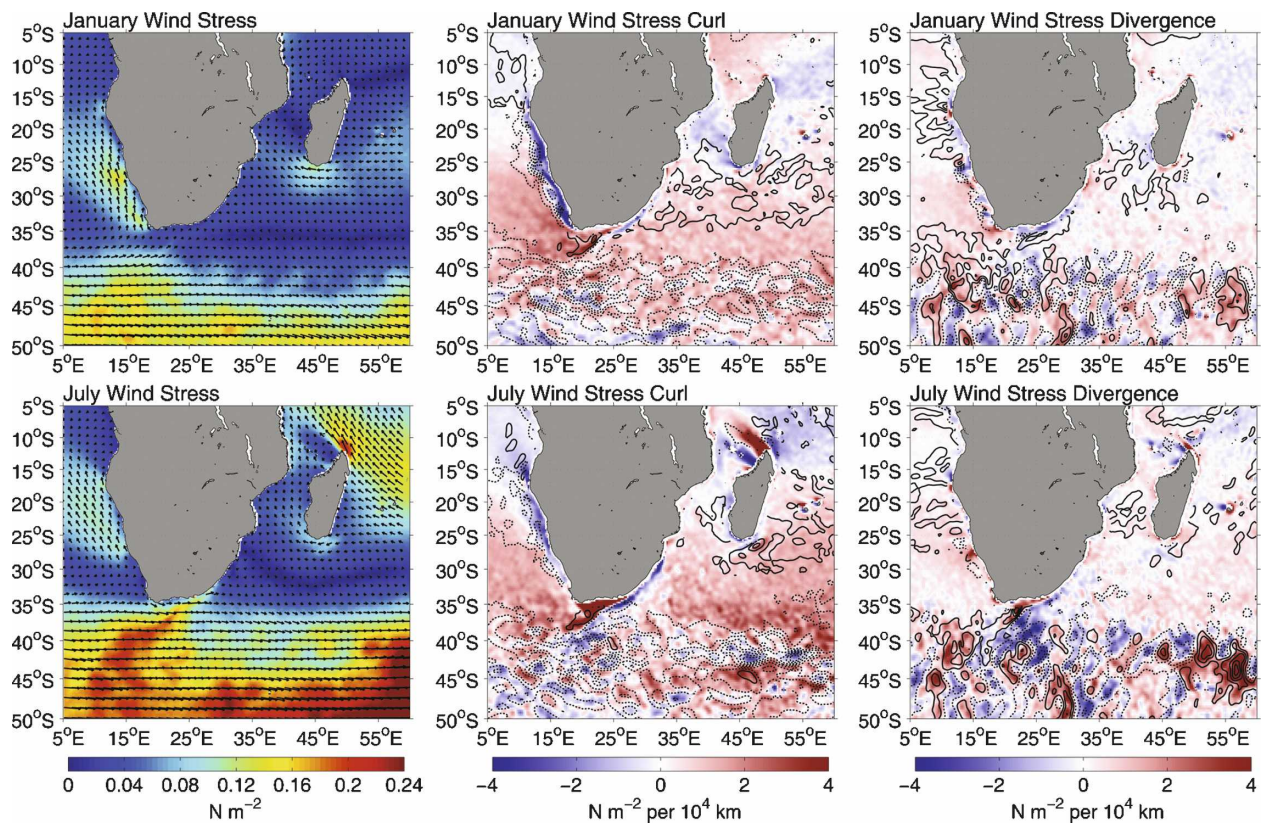


FIG. 14. Same as in Fig. 11, except for Southern Africa and Madagascar for January and July. Every fifth wind stress vector is plotted for clarity.

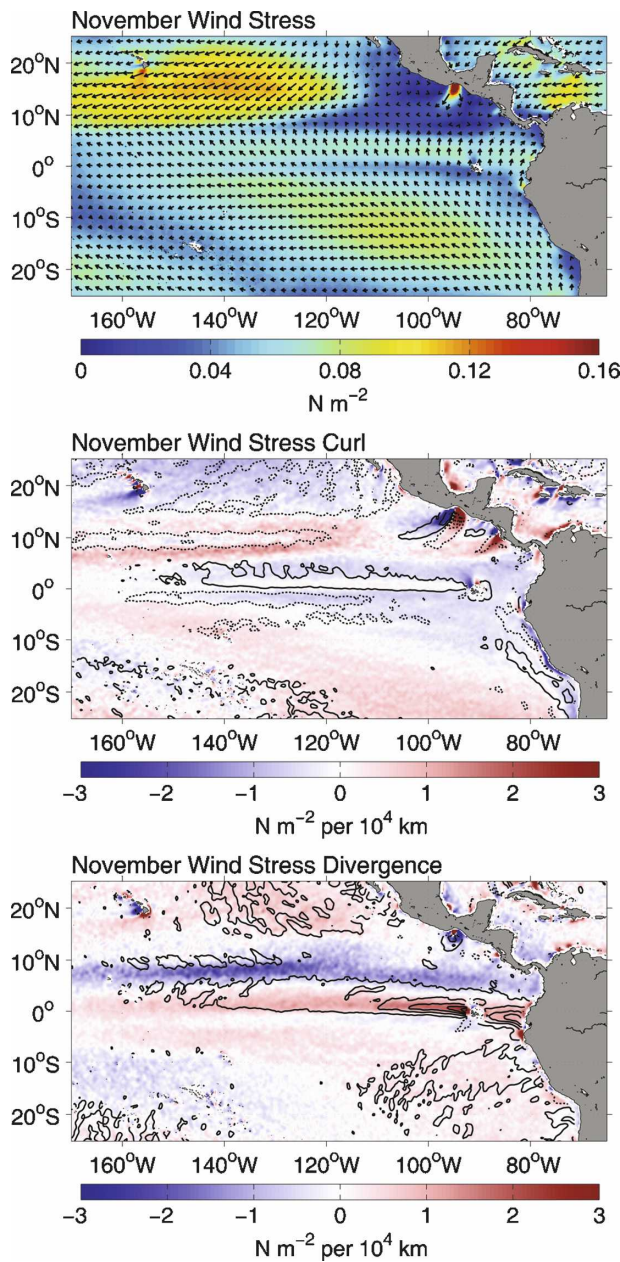


FIG. 15. Same as in Fig. 11, except for the eastern equatorial Pacific Ocean for November. Every eighth wind stress vector is plotted for clarity. Note the change in dynamic range for the wind stress and wind stress derivative fields.

latter regions show good correlations between positive (negative) wind stress curl and positive (negative) crosswind SST gradients (Fig. 12, middle). Similarly, the wind stress divergence field (Fig. 12, right) shows a strong relationship between positive (negative) wind stress divergence and positive (negative) downwind SST gradients. This is particularly true of the region between 35° and 49°S and 50° and 60°W. This corre-

sponds well with the results of Tokinaga et al. (2005), who found that SST fronts leave a clear signature in their 5-yr QuikSCAT wind-divergence climatology.

### 3) CALIFORNIA CURRENT SYSTEM

The late summertime wind stress field over the California Current System (CCS) is shown in Fig. 13. During summer and early fall, persistent northerly, upwelling-favorable wind stress dominates the CCS (Fig. 11, left). The wind stress field shows a broad-scale maximum of about  $0.14 \text{ N m}^{-2}$  from  $37.5^{\circ}\text{--}42.5^{\circ}\text{N}$ , and  $124^{\circ}\text{--}128^{\circ}\text{W}$ . Chelton et al. (2007) note similar broad-scale summertime intensifications in wind stress magnitude offshore of northern California and southern Oregon. Adjacent to the coast, the September wind stress curl field (Fig. 13, middle) is characterized by a narrow band of positive curl that stretches from Vancouver Island in the north to the southern tip of the Baja Peninsula. Local wind stress curl extrema occur off Vancouver Island, Cape Blanco, Cape Mendocino, in the Southern California Bight, and southeast of Cabo San Lucas. These features develop because of the SST influence on surface winds discussed above (Chelton et al. 2007). Offshore, the wind stress curl is generally negative. The influence of the wind shadow in the lee of Guadalupe Island ( $29^{\circ}\text{N}$ ,  $118.3^{\circ}\text{W}$ ) on the wind stress curl field is clearly evident, with regions of negative and positive curl located east and west of the island, respectively. Similar patterns in wind stress curl are observed in association with many other islands and island chains around the world (Chelton et al. 2004; Xie et al. 2001).

The influence of SST on the surface wind stress field is especially clear in the wind stress divergence field. The right-hand side of Fig. 13 shows the September wind stress divergence field in color with contours of AMSR-E downwind SST gradients overlaid. Zonal bands of positive and negative divergence can be seen extending more than 300 km from the coast in the region offshore of southern Oregon and northern California ( $36^{\circ}\text{--}41^{\circ}\text{N}$ ), a region that Castelao et al. (2006) show to be associated with high SST frontal activity during summer months. Here, bands of strongly positive (negative) wind stress divergence are collocated with regions of positive (negative) downwind temperature gradients. Using monthly summertime composites, Chelton et al. (2007) show the detailed structure of this coupling between downwind SST gradients and QuikSCAT wind stress divergence. Because of the differentiation, the 75-km gap in the AMSR-E data, discussed in section 2b, increases to about 100 km in the SST-gradient component fields computed from the  $0.25^{\circ}$ -gridded SST fields, thereby limiting AMSR-E-based investigation of the relationship between the

wind stress derivative fields and the SST gradient field close to the coast. From infrared-based SST analyses, Haack et al. (2008) show that this strong coupling between the SST field and the wind stress curl and divergence fields extends to within 20 km of the coast.

The influence of Guadalupe Island ( $29^{\circ}\text{N}$ ,  $118.5^{\circ}\text{W}$ ) on the surface wind field is again evident in the divergence field. A region of positive divergence north of Guadalupe Island indicates an area of difffluence upwind of the island. A region of convergence (negative divergence) south of the island indicates a confluence in the lee of the island. Two additional examples of this confluence/difffluence phenomenon are described in section 3d(4).

#### 4) SOUTHERN AFRICA AND MADAGASCAR

During the austral summer, the Benguela Current System (BCS) is strongly influenced by both the semi-permanent high pressure system known as the South Atlantic Anticyclone and the continental heat low that develops over the interior of southern Africa (Tyson and Preston-Whyte 2000). As the top of Fig. 14 shows, January winds tend to blow from the south-southeast over much of the region. A wedge-shaped region of strong wind stress extends from the Cape of Good Hope in the south to the central Namibian coast in the north. Local maxima of about  $0.13$  and  $0.15 \text{ N m}^{-2}$  occur near  $34^{\circ}\text{S}$ ,  $17^{\circ}\text{E}$  and  $26.5^{\circ}\text{S}$ ,  $14^{\circ}\text{E}$ , respectively. A secondary wind stress maximum ( $0.08 \text{ N m}^{-2}$ ) also occurs close to the coast at about  $17^{\circ}\text{S}$ ,  $11^{\circ}\text{E}$ .

Associated with this south-southeasterly wind stress is a band of strongly negative wind stress curl that runs the length of the coastline from  $15^{\circ}$  to  $34.5^{\circ}\text{S}$  (Fig. 14, top middle). In places, this band of negative wind stress curl extends more than 300 km offshore. The top middle of Fig. 14 shows a strong relationship between negative wind stress curl and negative crosswind SST gradients over the BCS.

The south-southeast wind stress described above drives offshore Ekman transport, which in turn drives the upwelling of cold nutrient-rich water onto the continental shelf (Peterson and Stramma 1991). Lutjeharms and Meeuwis (1987) identify eight regions of upwelling between  $10^{\circ}$  and  $35^{\circ}\text{S}$ . In association with these upwelling regions, the top right-hand side of Fig. 14 shows alternating regions of positive and negative wind stress divergence that result from the acceleration and deceleration of wind stress over regions of relatively warm and cold SST, respectively. This relationship is best illustrated at about  $26^{\circ}\text{S}$ , the approximate location of the Lüderitz upwelling cell (Lutjeharms and Meeuwis 1987), where negative downwind SST gradients are collocated with negative wind stress divergence. North

of the Lüderitz upwelling cell, positive downwind temperature gradients are collocated with positive wind stress divergence.

The austral winter (Fig. 14, bottom) brings with it significant changes for the BCS. The wedge of strong wind stress discussed above weakens and shifts north to about  $27^{\circ}\text{S}$ . Over the southern portion of the BCS, the influence of the westerly wind belt is clearly evident (Fig. 14, bottom left). During winter, the wind stress maximum at  $26.5^{\circ}\text{S}$ ,  $14^{\circ}\text{E}$  weakens to about  $0.12 \text{ N m}^{-2}$  while the maximum at  $17^{\circ}\text{S}$ ,  $11^{\circ}\text{E}$  strengthens to about  $0.11 \text{ N m}^{-2}$ . In association with these changes in the wind stress field, there are changes in the wind stress curl and divergence fields. The bottom middle of Fig. 14 shows a weakened band of negative wind stress curl that extends only as far south as about  $33^{\circ}\text{S}$ . Bakun and Nelson (1991) show a similar seasonal migration of wind stress curl. Additionally, the relationship between wind stress curl (divergence) and crosswind (downwind) SST gradients is less clear in July as a result of reduced upwelling.

The influence of the Agulhas Current on the wind stress curl fields is clearly visible along the east coast of South Africa in the January and July curl fields (Fig. 14, middle top and bottom, respectively). As is discussed above in section 3d(1) for the Gulf Stream, a couplet of parallel bands of positive and negative wind stress curl straddles the Agulhas Current after it separates from the coast south of South Africa, resulting from the fact that scatterometers measure the actual stress imposed on the sea surface by the wind. When viewed in the direction of flow, the Agulhas Current is manifest as parallel bands of negative and positive curl on the left- and right-hand sides of the current, respectively.

The Indian Ocean exhibits strong spatial and temporal variability in wind stress. This variability is associated with southwest (northeast) monsoon winds that blow during the boreal summer (winter) (Gadgil 2003). The onset of Southern Hemisphere winds associated with the Indian southwest monsoon is vividly illustrated in the bottom of Fig. 14 with the development of an intense corner acceleration of southeasterly winds off the northern tip of Madagascar, where wind stress magnitudes exceed  $0.2 \text{ N m}^{-2}$ . Local maxima are also visible in the bottom left-hand side of Fig. 14 south of Madagascar, showing a second weaker corner acceleration of easterly winds, and at about  $15^{\circ}\text{S}$ ,  $45.5^{\circ}\text{E}$  in the lee of a gap in the mountain range that runs north-south along the island. These features are much more apparent in the wind stress curl field (Fig. 14, bottom middle). This is particularly true of the gap wind, which is manifest as a localized region of negative wind stress

curl on the north side of the gap and a smaller region of positive wind stress curl on the south side of the gap.

East of Madagascar, the islands of Mauritius and Réunion provide two more examples of islands' influence on the surface wind field. The wind stress curl field (Fig. 14, bottom middle) shows positive (negative) extrema located north (south) of both islands. The wind stress divergence field (Fig. 14, bottom right) shows evidence of diffluence (positive divergence) upwind (east) of the islands and confluence (negative divergence) in the lee of the islands.

Poleward of  $35^{\circ}\text{S}$ , the influence of the meandering Agulhas Return Current (ARC), a region where annually averaged SST gradients can exceed  $4^{\circ}\text{C}$  ( $100 \text{ km}$ ) $^{-1}$  (O'Neill et al. 2005), on the surface wind stress field is clearly visible in Fig. 14. Westerly wind stress prevails year-round in this region with wind stress maxima exceeding  $0.24 \text{ N m}^{-2}$  in austral winter. As in all other regions, the influence of SST on surface winds as they blow across the ARC is especially clear in the wind stress divergence fields (Fig. 14, right) where regions of positive (negative) wind stress divergence are collocated with regions of positive (negative) downwind SST gradients. The relationship between wind stress curl (divergence) and crosswind (downwind) SST gradients strengthens in July. This is consistent with the findings of O'Neill et al. (2005), who noted a strong seasonal variability in the curl and divergence response to SST and that the surface wind stress response to SST gradients is significantly stronger during the austral winter than during the summer.

## 5) EASTERN EQUATORIAL PACIFIC OCEAN

A well-known feature of the eastern equatorial Pacific Ocean is the band of cold water near the equator that extends from South America west into the central equatorial Pacific. This so-called cold tongue exists with much seasonal (Mitchell and Wallace 1992) and interannual (Deser and Wallace 1990) variability. On average, the cold tongue persists from July to November and is most evident straddling the equator between  $95^{\circ}$  and  $125^{\circ}\text{W}$ . The top of Fig. 15 shows the deceleration of the southeasterly trade winds as they blow across the cold tongue into the ITCZ, which is located about  $9^{\circ}$  north of the equator. The wind stress magnitude decreases to about  $0.04 \text{ N m}^{-2}$  over the cold tongue and then increases rapidly north of the cold tongue as winds move over relatively warm SST. In November, the zonal bands of positive wind stress curl and divergence in the region  $0\text{--}5^{\circ}\text{N}$  and  $95\text{--}145^{\circ}\text{W}$  are collocated with regions of positive crosswind and downwind SST gradients, respectively. The wind stress and wind stress

curl and divergence patterns presented in Fig. 15 compare well with the findings of Chelton et al. (2001) and Chelton (2005).

Although November is not the period of strongest winds through the gaps in the Central American mountain range, the middle of Fig. 15 shows clear evidence of the Tehuantepec and Papagayo gap winds at about  $15^{\circ}\text{N}$ ,  $96^{\circ}\text{W}$  and  $11^{\circ}\text{N}$ ,  $87^{\circ}\text{W}$ , respectively (Bourassa et al. 1999; Chelton et al. 2000a,b; Xie et al. 2005). These wind jets are strongest in the wintertime. The Tehuantepec wind jet results from large ( $>5 \text{ hPa}$ ) cross-isthmus sea level pressure gradients that drive strong winds through the Chivela Pass and hundreds of kilometers into the eastern tropical Pacific (Chelton et al. 2000a). The Papagayo wind jet is driven by Caribbean trade winds (Chelton et al. 2000a). The top of Fig. 15 shows vector wind stress magnitudes of about  $0.25 \text{ N m}^{-2}$  for the Tehuantepec gap wind, known locally as *Tehuanos* (Trasviña et al. 1995), and  $0.06 \text{ N m}^{-2}$  for the Papagayo gap wind, called *Papagayos*. Wind stress magnitudes during individual events are significantly stronger than these climatological averages (Chelton et al. 2000a).

Associated with the Papagayos are two lobes of wind stress curl extending off the coast: a negative lobe on the poleward side of the wind jet and a stronger positive lobe on the equatorward side. A similar pattern of wind stress curl is produced by the Tehuanos (Fig. 15, middle), with the negative and positive lobes located west and east of the jet, respectively. An important difference between these two wind stress curl patterns is that the lobe of positive curl on the equatorward side of the Papagayos is adjacent to the band of positive curl on the northern side of the ITCZ (Kessler 2002). Both Xie et al. (2005) and Fiedler (2002) show for the months of February through April a shoaling of the thermocline from the Central American coast to about  $90^{\circ}\text{W}$ . This shoaling is associated with the annual cycle of the Costa Rica Dome centered near  $9^{\circ}\text{N}$ ,  $90^{\circ}\text{W}$  (Fiedler 2002) and results from the strong upwelling from Ekman pumping associated with the cyclonic wind stress curl generated by the Papagayos (Xie et al. 2005). The shoaling of the thermocline, combined with wind mixing, acts to inject nutrients into the surface layer. This region of high productivity supports a large zooplankton biomass as well as higher-trophic animals such as common dolphins (*Delphinus delphis*) and blue whales (*Balaenoptera musculus*) (Fiedler 2002).

Once again, individual islands such as the Galapagos near  $90^{\circ}\text{W}$  on the equator and island chains such as the Hawaiian Islands and French Polynesia, including the Marquesas Islands near  $10^{\circ}\text{S}$ ,  $140^{\circ}\text{W}$ , are seen to have

a profound influence on the surface wind field in the middle and bottom of Fig. 15.

#### 4. Conclusions

Seasonal cycles from a Scatterometer-based Climatology of Ocean Winds (SCOW) have been estimated by harmonic analysis for 12 different wind variables from 8 yr of QuikSCAT observations. The details of the methodology used to construct these seasonal cycles are described in section 2 and the results are presented in section 3 for the three wind variables that are of most interest to ocean circulation studies (the wind stress, wind stress curl, and wind stress divergence). In practice, seasonal cycles computed by harmonic analysis generally differ little from seasonal cycles computed as long-term averages for each calendar month (see appendix C). For the 8-yr QuikSCAT data record analyzed here, harmonic analysis is preferable to long-term averages because it is less susceptible to spurious effects from highly anomalous winds during one or more months. Moreover, harmonic analysis has the advantage that the seasonal value can easily be obtained from the regression coefficients at arbitrary time intervals, for example, the short integration time step used in numerical ocean circulation models.

The SCOW climatology differs from our previous Climatology of Global Ocean Winds (COGOW; Risien and Chelton 2006), which is a Web-based interactive atlas that allows users to retrieve climatological average wind statistics (relative frequency of wind speed and direction) for each calendar month for any desired location on a  $0.5^\circ \times 0.5^\circ$  global grid in both tabular and graphical (wind rose) form. COGOW was designed to meet the operational needs of oil spill and search and rescue responders, for example, at particular locations and cannot be easily adapted to provide the gridded wind fields needed by ocean modelers to force ocean models, because the COGOW database must be accessed grid point by grid point.

SCOW also differs from the global high-wind-speed climatology ( $>20 \text{ m s}^{-1}$ ) recently presented by Sampe and Xie (2007) based on 7 yr of QuikSCAT observations, which is intended to provide statistical information on extreme wind conditions.

The high spatial resolution of the SCOW seasonal cycles of the wind fields are designed to meet the needs of the ocean modeling and hydrographic research communities. The extensive coverage of the QuikSCAT data from which SCOW was constructed (two or more observations per day over most of the World Ocean) contrasts with the sparse coverage of in situ observations over much of the World Ocean by buoys and ships

that have been used in previous observationally based ocean wind climatologies (Hellerman and Rosenstein 1983; Da Silva et al. 1994; Josey et al. 2002; Fig. 1; see also Fig. 1 of Risien and Chelton 2006). Global ocean wind climatologies have been produced from the output of numerical weather prediction models (e.g., Trenberth et al. 1990; see also the NCEP–NCAR reanalysis climatology in sections 3a–3c) in an effort to address the coverage limitations of ship and buoy observations, but these model-based wind climatologies are compromised by the poor resolution of the model wind fields that limits the resolution to features larger than several hundred kilometers (Milliff et al. 2004; Chelton et al. 2004), as well as by issues related to model physics. The much higher resolution of the SCOW wind fields reveals numerous small-scale and seasonally recurring features in the wind field that are poorly resolved or completely absent in any of the previous observationally based or model-based wind climatologies.

Although we believe the SCOW climatology is superior to any other existing climatologies of ocean winds because of its much higher spatial resolution, the limitations of the SCOW climatology should be kept in mind. Probably most significantly, SCOW is limited as are all seasonal cycle climatologies by the fact that the seasonal cycle accounts for only a small percentage of the total variance of winds at most locations. Most of the wind variance occurs on time scales between about a day and about a week in association with the synoptic weather variability. Fortunately, the ocean is generally less responsive to the synoptic variability of the wind field that is poorly resolved in satellite and in situ observations than it is to more slowly varying wind forcing. But even in monthly averages, the seasonal cycle accounts for a relatively small percentage of the monthly average variability in most locations because of large year-to-year variations (see Figs. 3, C1). The seasonal cycle of wind forcing has nonetheless proven useful in many previous ocean modeling studies. While limitations of the utility of the seasonal cycle are applicable to all available wind climatologies, the 8-yr duration of the QuikSCAT data record is shorter than the data records from which other climatologies have been constructed. This disadvantage of SCOW is largely offset, however, by the much higher spatial resolution of SCOW compared with all other wind climatologies.

Another potential concern with the SCOW climatology is that the diurnal cycle is not fully resolved by the QuikSCAT observations. A given location on the sea surface is usually sampled twice per day at midlatitudes (once on an ascending orbit and once on a descending orbit) with a time separation of about 12 h. Because of overlap of measurement swaths from successive orbits,

the number of samples per day is greater at latitudes higher than about  $50^{\circ}$  and the sampling rate can be less than twice per day at low latitudes where the satellite ground tracks are more widely spaced. Twice-daily observations barely resolve the  $1 \text{ cycle day}^{-1}$  frequency. Any higher harmonics of this fundamental diurnal frequency will be aliased at midlatitudes, and even the fundamental frequency can be aliased at low latitudes where the sampling is less than twice per day. The effects of this aliasing are mitigated to some extent by the monthly averaging and harmonic analysis used to obtain the seasonal cycles of the various wind fields. The residual effects of this aliasing are probably small in most regions, but may be a concern near land and in the trade winds where the diurnal cycles are significant (Gille et al. 2005). Quantifying these residual aliasing effects would be very difficult.

One other important distinction between SCOW and other wind climatologies is that the wind stresses in the SCOW climatology are the true wind stress on the sea surface, which is determined by the difference between the wind velocity and the surface velocity of the ocean (Cornillon and Park 2001; Kelly et al. 2001; Chelton et al. 2004). The winds from other climatologies should be adjusted to account for the effects of surface ocean currents when computing the stress on the sea surface (Pacanowski 1987; Dawe and Thompson 2006), but this is seldom done in practice.

While only the wind stress and wind stress derivative fields in SCOW are addressed here, monthly global maps (January–December) constructed from the annual and semiannual harmonics for these and nine other wind variables, as well as the regression coefficients from which the monthly values were computed, can be downloaded (available online at <http://cioss.coas.oregonstate.edu/scow>). These regression coefficients allow easy calculation of the seasonal cycles at arbitrary time intervals (e.g., the small time step in ocean circulation models). The 12 variables in the SCOW climatology are wind speed, wind speed squared, wind speed cubed, zonal and meridional wind components, wind curl and divergence, wind stress magnitude, zonal and meridional wind stress components, and wind stress curl and divergence.

For researchers interested in more than just the annual and semiannual harmonics, the regression coefficients for the higher-order three- and four-cycles-per-year harmonics are available for each variable at the above Web address. Using these coefficients and the example code provided on the Web site, seasonal cycles can thus be constructed from up to four harmonics, with a temporal resolution that best suits individual needs.

Numerous examples of seasonally recurring and dy-

namically important small-scale features in the SCOW global ocean wind fields are presented in section 3d. These features are especially evident in the wind stress derivative fields from which orographic, SST gradient and ocean current influences on the surface winds are clearly visible. Because SCOW captures small-scale features that are not resolved in any previous observationally based or model-based wind atlases or in the NCEP–NCAR reanalysis fields (bottom of Figs. 6 and 8), we expect that SCOW will prove valuable to many researchers conducting hydrographic and ocean modeling studies. Representativeness errors in the present SCOW climatology because of the limited 8-yr QuikSCAT data record will be addressed in the future by incorporating additional QuikSCAT observations as they become available, as well as observations from other scatterometer missions.

**Acknowledgments.** We thank two reviewers and Carl Wunsch for comments that improved the manuscript. We also thank Michael Schlax for QuikSCAT data-processing support. NOC data were obtained from the National Oceanography Centre, Southampton (<http://www.noc.soton.ac.uk/JRD/MET/fluxclimind.php>). NCEP–NCAR reanalysis winds were provided by NOAA/OAR/ESRL PSD, Boulder, Colorado (from their Web site at <http://www.cdc.noaa.gov/>). The ICOADS data in Fig. 1 were obtained from the NOAA Earth System Research Laboratory (<http://www.cdc.noaa.gov/cdc/data.coads.1deg.html>). This research was conducted with support from NASA Grant NAS5-32965 for funding of Ocean Vector Winds Science Team activities and Award NA03NES4400001 to Oregon State University's Cooperative Institute for Oceanographic Satellite Studies from the National Oceanic and Atmospheric Administration, U.S. Department of Commerce. The statements, findings, conclusions, and recommendations expressed here are those of the authors and do not necessarily reflect the views of the National Oceanic and Atmospheric Administration, the U.S. Department of Commerce, or the National Aeronautics and Space Administration.

## APPENDIX A

### Sampling Errors in the NOC Wind Stress Climatology

On large scales, ocean dynamics are governed by conservation of angular momentum. As a consequence, the aspect of the wind field that forces the large-scale ocean circulation in the open ocean away from coastal boundaries is the curl of the wind stress, rather than the

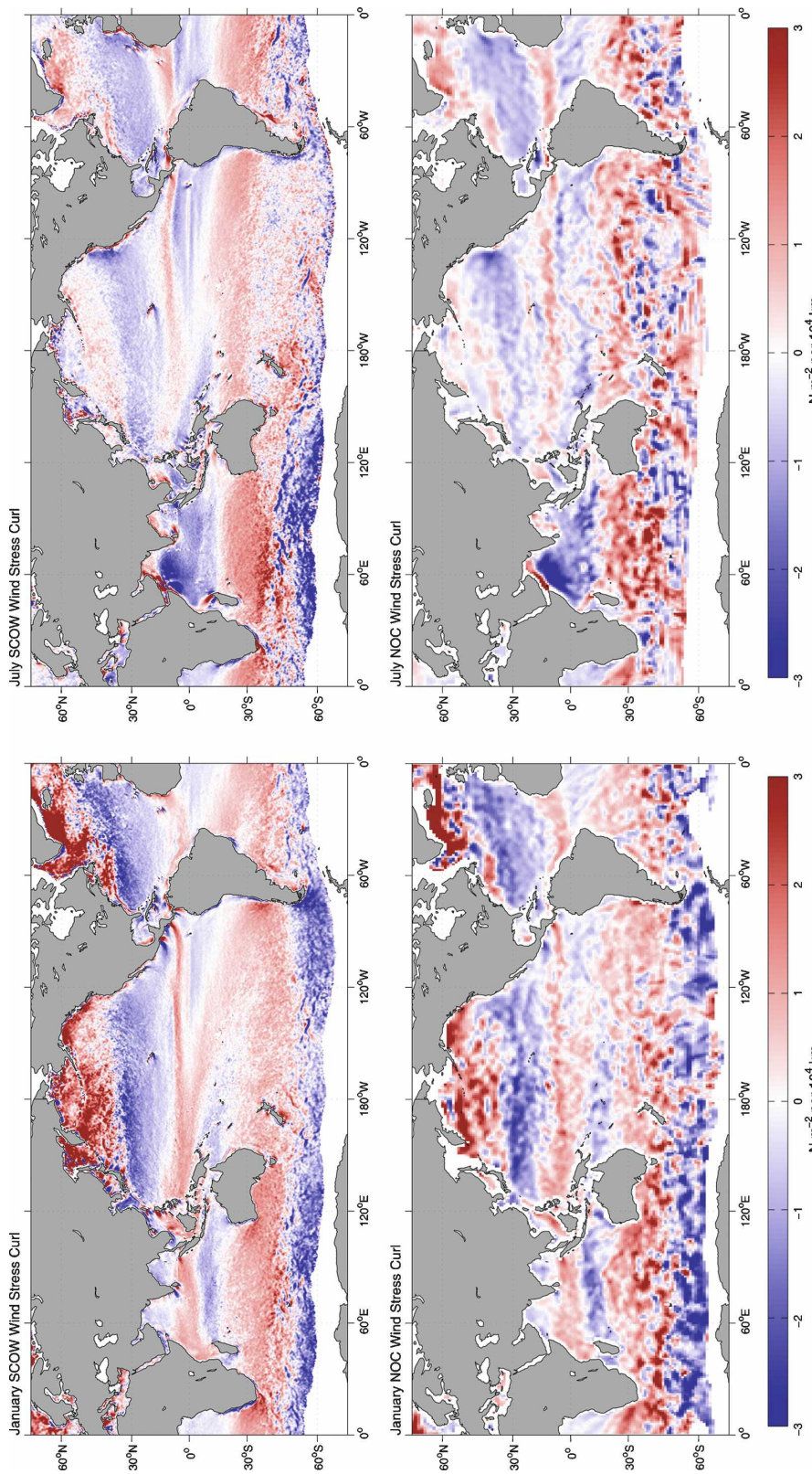


FIG. A1. (top) Global SCOW and (bottom) NOC wind stress curl maps for (left) January and (right) July. The SCOW fields are plotted on a  $0.25^\circ \times 0.25^\circ$  grid. The NOC fields are plotted on the  $1^\circ \times 1^\circ$  grid of the NOC climatology.

wind stress itself. Thus, although the wind forcing is imposed as the vector wind stress at the sea surface in ocean models, the model responds to the wind stress curl. The accuracy of the wind stress curl is therefore of fundamental importance to ocean dynamics. This is a rather stringent consideration given that the derivatives of the curl operator effectively act as a spatial high-pass filter, thus emphasizing any sampling errors that may exist in a wind stress climatology. Subtle sampling errors in the wind stress fields can become very apparent in the wind stress curl climatology.

The global wind stress curl fields from SCOW and computed from the NOC wind stress climatology are shown in Fig. A1 for the months of January and July. The small-scale features in the SCOW curl fields in the top two panels are due to a variety of influences, as summarized in detail in section 3. The most notable features of Fig. A1 are the “splotchy” patterns in the NOC curl fields in the bottom two panels. These nonphysical features are evident year-round in the Southern Hemisphere and at the mid- and high-latitudes of the Northern Hemisphere in the wintertime. They are attributable to the coarse sampling of the ship observations from which the NOC climatology is computed.

While the NOC climatology may be of considerable value for studies of long-term year-to-year variability in the well-sampled regions of the ocean, it is quite probable that the spurious structures in the NOC wind stress curl climatology would generate locally spurious features in the ocean circulation in models forced by the NOC wind stress fields. As shown in Fig. 10, they also lead to systematic errors in the zonally integrated wind stress curl that provides a rough estimate of the western boundary current transports associated with the large-scale ocean circulation from Sverdrup dynamics, as discussed in section 3c. Because of the dense spatial and temporal sampling of the QuikSCAT observations over the 8-yr data record, the SCOW climatology is free of these large sampling errors that are evident in the ship-based NOC climatology. The primary limitation of the SCOW climatology is the relatively short 8-yr duration of the QuikSCAT data record from which the climatology was constructed.

We note that it may be useful to exploit the complementary nature of the QuikSCAT (high spatial resolution and complete coverage) and in situ data (long time series with inhomogeneous spatial coverage) to derive estimates of long time series of indices for small-scale variability of the wind field based on statistical relations developed from analysis of the two datasets during the overlap period since July 1999. Such analyses are beyond the scope of the present study.

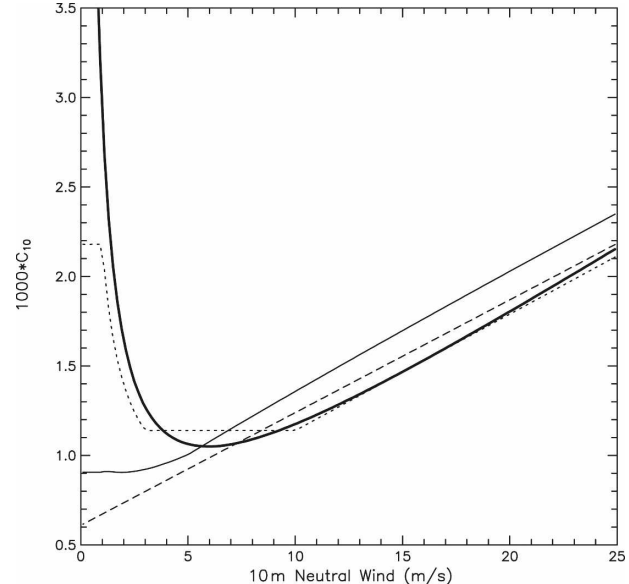


FIG. B1. The wind speed dependence of drag coefficients for neutrally stable conditions: the 1994 modified Large and Pond formulation described in the appendix of Large et al. (1994) (thick solid line); the 1990 modified Large and Pond formulation described by Trenberth et al. (1990) (dotted line); the Smith (1980) formulation (dashed line); and the COARE 3.0 formulation presented by Fairall et al. (2003) (thin solid line).

## APPENDIX B

### Wind Stress Drag Coefficient Formulation

The vector wind stress  $\tau$  in the SCOW climatology is computed from QuikSCAT observations of the equivalent neutral stability vector winds at 10 m,  $\mathbf{v}_{10}$ , (see section 2a) based on the bulk aerodynamic formula, which is given by

$$\tau = \rho C_{10} \mathbf{v}_{10} |\mathbf{v}_{10}|,$$

where  $\rho$  is the air density (taken here to be  $1.223 \text{ kg m}^{-3}$ ) and  $C_{10}$  is the drag coefficient for neutrally stable conditions. The accuracy of wind stress estimated in this manner is clearly dependent on the specification of the drag coefficient. Several formulations are in common use, and there is no general agreement on which specification is most accurate.

The wind stress fields in the SCOW climatology were computed using the modified Large and Pond drag coefficient described in the appendix of Large et al. (1994), which is the formulation most commonly used for scatterometer applications. This wind speed-dependent drag coefficient is shown as the heavy solid line in Fig. B1. Three other commonly used formulations for the drag coefficient are also shown in the fig-

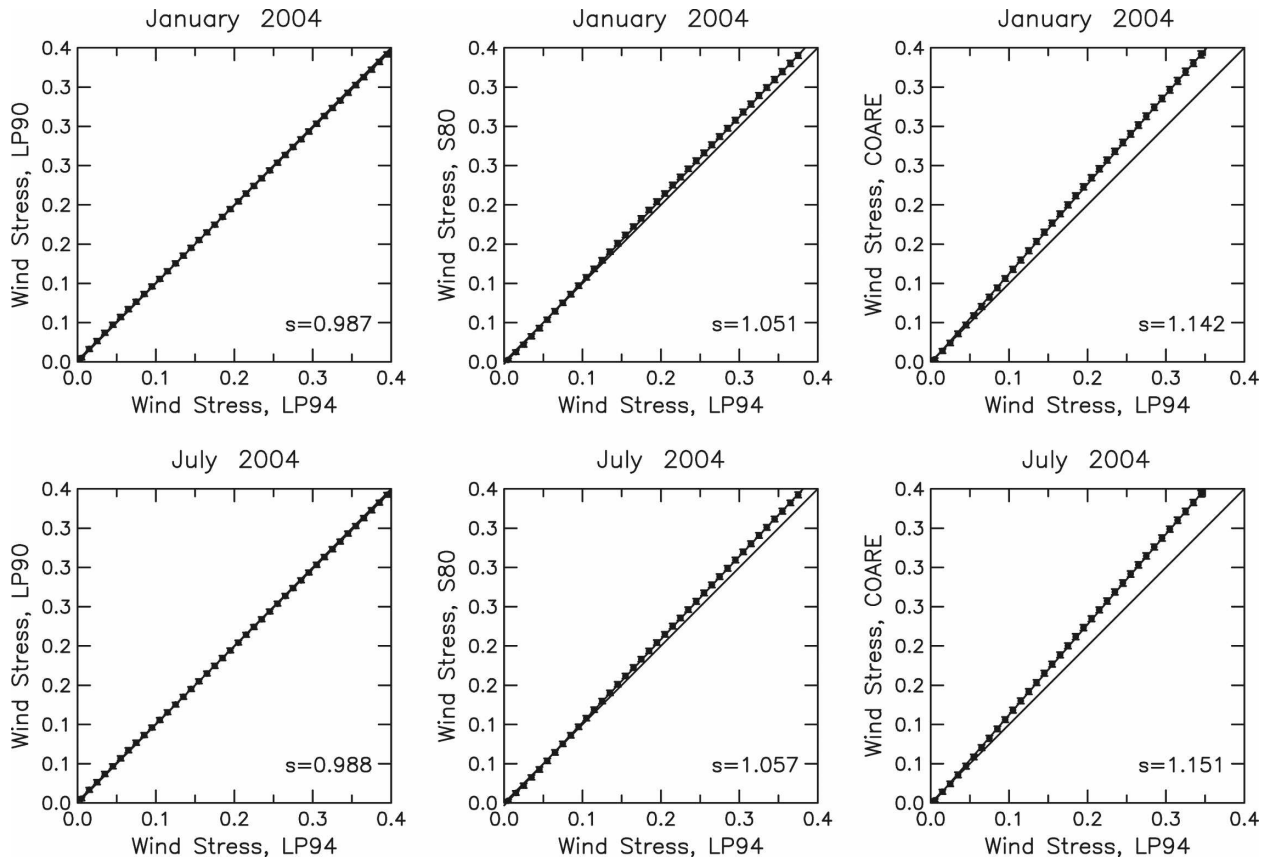


FIG. B2. Binned scatterplots showing the relationships between the magnitudes of the wind stress computed here using the 1994 modified Large and Pond drag coefficient (LP94) described in the appendix of Large et al. (1994) and various other drag coefficient formulations for January 2004 and July 2004 monthly average on a global  $0.25^\circ \times 0.25^\circ$  grid. (left to right) The 1990 modified Large and Pond drag coefficient described by Trenberth et al. (1990) (LP90); the Smith (1980) drag coefficient (S80); and the polynomial form of the COARE 3.0 drag coefficient presented by Kara et al. (2005) (COARE). The mean value in each bin is shown by a dot, and the std dev of the values in each bin is shown by vertical bars that are barely discernable because the scatter within each bin is so small. In each panel, the least squares fit line is drawn through the mean values in the bins and the line of perfect agreement is shown by a diagonal line. The slope of the least squares fit straight line is labeled in the lower right-hand corner of each panel.

ure. The differences between the Trenberth et al. 1990 and Large et al. 1994 modifications of the Large and Pond drag coefficient are relatively small for wind speeds higher than  $1 \text{ m s}^{-1}$ . For moderate to high wind speeds (greater than about  $6 \text{ m s}^{-1}$ ), it is readily apparent that the Smith (1980) drag coefficient is somewhat larger than the modified Large and Pond formulations and that the COARE 3.0 drag coefficient (Fairall et al. 2003) is systematically larger than any of the other formulations.

The impact of the various drag coefficient formulations on the monthly mean wind stresses analyzed for this study are shown in Fig. B2 for the months of January and July 2004. In all cases, the differences are very robust. The monthly average wind stress magnitude fields computed from the Trenberth et al. 1990 modification of the Large and Pond drag coefficient are about

1% weaker than those computed from the Large et al. 1994 modification of the Large and Pond drag coefficient used to produce the SCOW climatology. The Smith (1980) and COARE 3.0 drag coefficients yield monthly average wind stress magnitude fields that are about 5% stronger and 15% stronger, respectively, than the 1994 modified Large and Pond drag coefficient.

The standard deviations of the values within each bin in Fig. B2 are very small in all cases. Users who prefer any of the other three drag coefficient formulations considered here can thus obtain accurate estimates of the wind stress fields that would be obtained with their preferred formulation by multiplying the SCOW climatological average stresses by 0.99, 1.05, and 1.15 for the 1990 modified Large and Pond drag coefficient, the Smith (1980) drag coefficient, and the COARE 3.0 drag coefficient, respectively.

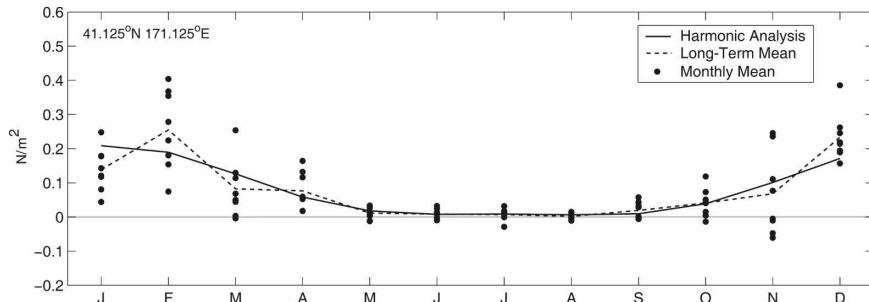


FIG. C1. An example showing the differences between the climatological seasonal cycles computed from the QuikSCAT winds by harmonic analysis with two harmonics (annual and semiannual, solid line) and as long-term means from arithmetic averages for each month (dashed line). The eight individual monthly mean values for each calendar month are shown by dots. The location of this example ( $41.125^{\circ}\text{N}$ ,  $171.125^{\circ}\text{E}$ ) corresponds to the region of largest RMS differences between the two seasonal cycles.

## APPENDIX C

### Harmonic Analysis versus Long-Term Average Seasonal Cycles

The traditional method for computing climatological seasonal cycles is to compute long-term means for each of the 12 calendar months from the arithmetic average of all available observations in each month. For long data records, the resulting seasonal cycle is usually stable. As the duration of the data record (i.e., the number of values included in the arithmetic averages) decreases, the long-term average becomes more susceptible to spuriously large values that can arise either from measurement errors or from sampling errors due to highly anomalous geophysical conditions during a particular month in one or more years. Sampling errors can be particularly severe if the observations are not sampled evenly over the data record. The ship observations in the NOC climatology, for example, are very unevenly distributed over the 46-yr dataset from which the long-term averages were computed (see Figs. 1b,c). At high southern latitudes, it is not uncommon to find only a single observation in a given month and year. If this observation was made during anomalous conditions (e.g., during a storm or an unusually calm period), it would have undue influence on the arithmetic average for that month.

For the QuikSCAT-based SCOW climatology presented here, measurement errors are generally not a problem, except for possible rain- or ice-contaminated observations that were not detected in the data processing and possible aliasing of diurnal variability that is at best marginally resolved by QuikSCAT observations and can be significant within a few hundred kilometers of land and in the trade wind belts (Gille et al. 2005).

The effects of rain contamination and aliasing are largely mitigated by the monthly averaging and harmonic analysis used here to estimate the seasonal cycles. Likewise, sampling errors are relatively small because the wind observations are very evenly spaced over the 8-yr duration of the QuikSCAT data record. In some cases, however, sampling errors can still be somewhat problematic. For example, an unusually stormy month in a particular year could result in an uncharacteristic large monthly mean value that could skew the long-term arithmetic average for that month.

The effects of both measurement and sampling errors can be mitigated by computing the climatological seasonal cycle by harmonic analysis, as described in section 2d. In this case, the undue influence of spurious values are reduced by the fact that regression of the complete time series (8 yr, in the case of SCOW) effectively utilizes nearby monthly mean values to reduce the spurious effect of any individual monthly average.

An example of the advantages of harmonic analysis over long-term averages is shown in Fig. C1 for the zonal wind stress in a region of the North Pacific where the root-mean-square differences between the two climatological seasonal cycles are the largest anywhere in the World Ocean. In this case, the spread of the eight individual monthly means is larger during the months of February and November than during the other months. Because the mean value is not well defined from such a small number of observations, the long-term average values for these months introduces irregularity in the seasonal cycle (dashed line). The relatively high values for February and low values for November are not likely recurring features of the seasonal cycle. In any case, a longer data record would be required to ascertain whether these irregularities in the seasonal cycle are meaningful. The harmonic seasonal cycle

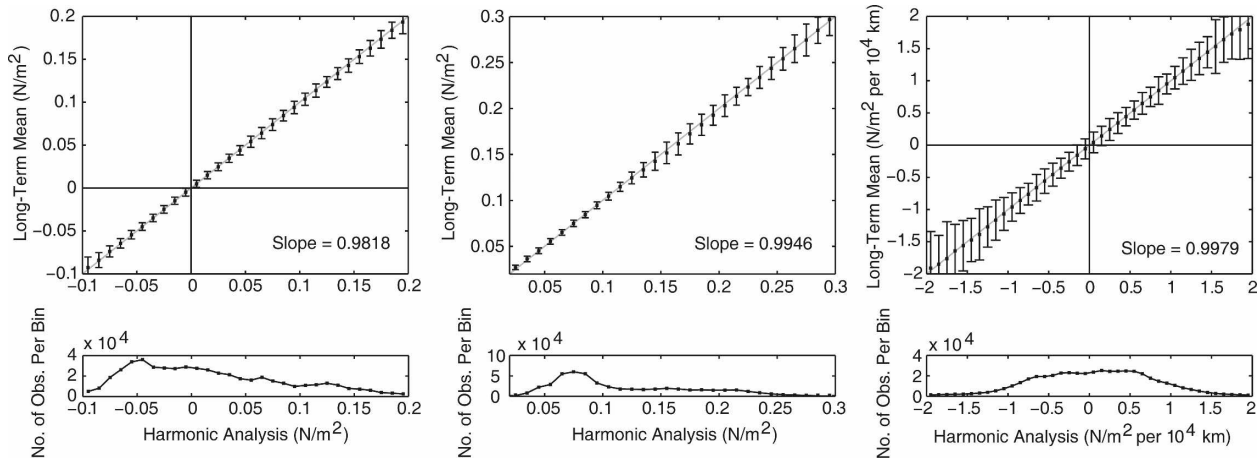


FIG. C2. Binned scatterplots showing the relationships between climatological seasonal cycles computed from the QuikSCAT winds by harmonic analysis with two harmonics (annual and semiannual) and as long-term means from arithmetic averages for each month. (left to right) Zonal wind stress, wind stress magnitude, and wind stress curl. The mean value in each bin is shown by a dot and the std dev of the values in each bin is shown by the vertical bars. The slopes of the least squares fit lines through the means are labeled in the lower right-hand corner of the top panels. The bottom panels show the distributions of the harmonic seasonal cycle values within each bin. The larger std devs at the tails of the distributions reflect the smaller sample sizes in these bins.

(solid line) is not significantly affected by these sampling issues.

In addition to mitigating the effects of sampling errors, harmonic analysis has the advantage that the seasonal cycle can be computed for any specified time during the year at any time interval (e.g., the short integration time step used in numerical models). For climatological seasonal cycles specified by the long-term averaging method, some interpolation scheme is necessary to specify the seasonal cycle at time steps shorter than the monthly intervals at which the long-term averages are computed.

For the case of the SCOW climatology, our preference for harmonic analysis to estimate the climatological seasonal cycle rather than long-term averages is not a major issue. As shown by the binned scatterplots in Fig. C2 for the zonal wind stress, wind stress magnitude, and wind stress curl, the long-term averages are very similar to the monthly values from harmonic analysis with two harmonics (annual plus semiannual). In all three cases, the slopes of the least squares fit lines through the mean value in each bin does not differ significantly from 1. The standard deviation within each bin is small over the range of values that are well sampled. The larger standard deviations at the extremes of the distributions of values are due to the small sample size in those bins.

#### REFERENCES

- Bakun, A., and C. S. Nelson, 1991: The seasonal cycle of wind stress curl in subtropical eastern boundary current regions. *J. Phys. Oceanogr.*, **21**, 1815–1834.
- Böttger, H., 1982: Local element guidance from the ECMWF forecasting system in the medium range. A verification study. *Proc. Statistical Interpretation of Numerical Weather Prediction Products Seminar/Workshop*, Reading, United Kingdom, ECMWF, 417–441.
- Bourassa, M. A., L. Zamudio, and J. J. O'Brien, 1999: Non-inertial flow in NSCAT observations of Tehuantepec winds. *J. Geophys. Res.*, **104**, 11 311–11 320.
- Castelao, R. M., T. P. Mavor, J. A. Barth, and L. C. Breaker, 2006: Sea surface temperature fronts in the California Current System from geostationary observations. *J. Geophys. Res.*, **111**, C09026, doi:10.1029/2006JC003541.
- Chelton, D. B., 2005: The impact of SST specification on ECMWF surface wind stress fields in the eastern tropical Pacific. *J. Climate*, **18**, 530–550.
- , and M. H. Freilich, 2005: Scatterometer-based assessment of 10-m wind analyses from the operational ECMWF and NCEP numerical weather prediction models. *Mon. Wea. Rev.*, **133**, 409–429.
- , and F. J. Wentz, 2005: Global microwave satellite observations of sea surface temperature for numerical weather prediction and climate research. *Bull. Amer. Meteor. Soc.*, **86**, 1097–1115.
- , A. M. Mestas-Núñez, and M. H. Freilich, 1990: Global wind stress and Sverdrup circulation from the Seasat scatterometer. *J. Phys. Oceanogr.*, **20**, 1175–1205.
- , M. H. Freilich, and S. K. Esbensen, 2000a: Satellite observations of the wind jets off the Pacific coast of Central America. Part I: Case studies and statistical characteristics. *Mon. Wea. Rev.*, **128**, 1993–2018.
- , —, and —, 2000b: Satellite observations of the wind jets off the Pacific coast of Central America. Part II: Regional relationships and dynamical considerations. *Mon. Wea. Rev.*, **128**, 2019–2043.
- , and Coauthors, 2001: Observation of coupling between surface wind stress and sea surface temperature in the eastern tropical Pacific. *J. Climate*, **14**, 1479–1498.
- , M. G. Schlax, M. H. Freilich, and R. F. Milliff, 2004: Satellite

- measurements reveal persistent small-scale features in ocean winds. *Science*, **303**, 978–983.
- , M. H. Freilich, J. M. Sienkiewicz, and J. M. Von Ahn, 2006: On the use of QuikSCAT scatterometer measurements of surface winds for marine weather prediction. *Mon. Wea. Rev.*, **134**, 2055–2071.
- , M. G. Schlax, and R. M. Samelson, 2007: Summertime coupling between sea surface temperature and wind stress in the California Current System. *J. Phys. Oceanogr.*, **37**, 495–517.
- Cornillon, P., and K.-A. Park, 2001: Warm core ring velocities inferred from NSCAT. *Geophys. Res. Lett.*, **28**, 575–578.
- da Silva, A. M., C. C. Young, and S. Levitus, 1994: *Algorithms and Procedures*. Vol. 1, *Atlas of Surface Marine Data*, NOAA Atlas NESDIS 6, 74 pp.
- Dawie, J. T., and L. Thompson, 2006: Effect of ocean surface currents on wind stress, heat flux, and wind power input to the ocean. *Geophys. Res. Lett.*, **33**, L09604, doi:10.1029/2006GL025784.
- Deser, C., and J. M. Wallace, 1990: Large-scale atmospheric circulation features of warm and cold episodes in the tropical Pacific. *J. Climate*, **3**, 1254–1281.
- de Szoeke, R. A., 1987: On the wind-driven circulation of the South Pacific Ocean. *J. Phys. Oceanogr.*, **17**, 613–630.
- Doyle, J. D., and M. A. Shapiro, 1999: Flow response to large-scale topography: The Greenland tip jet. *Tellus*, **51A**, 728–748.
- Fairall, C. W., E. F. Bradley, J. E. Hare, A. A. Grachev, and J. B. Edson, 2003: Bulk parameterization of air-sea fluxes: Updates and verification for the COARE algorithm. *J. Climate*, **16**, 571–591.
- Fiedler, P. C., 2002: The annual cycle and biological effects of the Costa Rica Dome. *Deep-Sea Res.*, **49A**, 321–338.
- Freilich, M. H., D. G. Long, and M. W. Spencer, 1994: SeaWinds: A scanning scatterometer for ADEOS II—Science overview. *Proc. Int. Geoscience and Remote Sensing Symp.*, Pasadena, CA, IEEE, 960–963.
- Gadgil, S., 2003: The Indian monsoon and its variability. *Annu. Rev. Earth Planet. Sci.*, **31**, 429–467.
- Garzoli, S. L., 1993: Geostrophic velocities and transport variability in the Brazil/Malvinas confluence. *Deep-Sea Res.*, **40**, 1379–1403.
- Gibson, J. K., P. Källberg, S. Uppala, A. Noumura, A. Hernandez, and E. Serrano, 1997: ERA description. ECMWF Re-analysis Project Rep. Series 1, ECMWF, 77 pp.
- Gille, S. T., S. G. Llewellyn Smith, and N. M. Statom, 2005: Global observations of the land breeze. *Geophys. Res. Lett.*, **32**, L05605, doi:10.1029/2004GL022139.
- Godfrey, J. S., 1989: A Sverdrup model of the depth-integrated flow for the world ocean allowing for island circulations. *Geophys. Astrophys. Fluid Dyn.*, **45**, 89–112.
- Goni, G., S. Kamholz, S. Garzoli, and D. Olson, 1996: Dynamics of the Brazil-Malvinas Confluence based on inverted echo sounders and altimetry. *J. Geophys. Res.*, **101**, 16 273–16 289.
- Gordon, C., and R. A. Corry, 1991: A model simulation of the seasonal cycle in the tropical Pacific Ocean using climatological and modeled surface forcing. *J. Geophys. Res.*, **96**, 847–864.
- Haack, T., D. B. Chelton, J. Pullen, J. D. Doyle, and M. G. Schlax, 2008: Summertime influence of SST on surface wind stress off the U.S. West Coast from the U.S. Navy COAMPS model. *J. Phys. Oceanogr.*, **38**, 2414–2437.
- Harrison, D. E., 1989: On climatological monthly mean wind stress and wind stress curl fields over the World Ocean. *J. Climate*, **2**, 57–70.
- Hashizume, H., S.-P. Xie, W. T. Liu, and K. Takeuchi, 2001: Local and remote atmospheric response to tropical instability waves: A global view from space. *J. Geophys. Res.*, **106**, 10 173–10 186.
- Hellerman, S., and M. Rosenstein, 1983: Normal monthly wind stress over the World Ocean with error estimates. *J. Phys. Oceanogr.*, **13**, 1093–1104.
- Huang, R. X., W. Wang, and L. L. Liu, 2006: Decadal variability of wind energy input to the world ocean. *Deep-Sea Res. II*, **53**, 31–41.
- Huddleston, J. N., and B. W. Stiles, 2000: Multidimensional histogram (MUDH) rain flag product description (version 3.0). Jet Propulsion Laboratory Tech. Rep., 8 pp. [Available online at [ftp://podaac.jpl.nasa.gov/pub/ocean\\_wind/quikscat/L2B/doc/MUDH\\_Description\\_V3.pdf](ftp://podaac.jpl.nasa.gov/pub/ocean_wind/quikscat/L2B/doc/MUDH_Description_V3.pdf).]
- Janssen, P. A. E. M., P. Lionello, M. Reistad, and A. Hollingsworth, 1989: Hindcasts and data assimilation studies with the WAM model during the Seasat period. *J. Geophys. Res.*, **95**, 13 483–13 496.
- Josey, S. A., E. C. Kent, and P. K. Taylor, 2002: Wind stress forcing of the ocean in the SOC climatology: Comparisons with the NCEP–NCAR, ECMWF, UWM/COADS, and Hellerman and Rosenstein datasets. *J. Phys. Oceanogr.*, **32**, 1993–2019.
- Kalnay, E., and Coauthors, 1996: The NCEP/NCAR 40-Year Reanalysis Project. *Bull. Amer. Meteor. Soc.*, **77**, 437–471.
- Kara, A. B., H. E. Hurlbert, and A. J. Wallcraft, 2005: Stability-dependent exchange coefficients for air-sea fluxes. *J. Atmos. Oceanic Technol.*, **22**, 1080–1094.
- Kelly, K. A., S. Dickenson, M. J. McPhaden, and G. C. Johnson, 2001: Ocean currents evident in satellite wind data. *Geophys. Res. Lett.*, **28**, 2469–2472.
- Kessler, W. S., 2002: Mean three-dimensional circulation in the northeast tropical Pacific. *J. Phys. Oceanogr.*, **32**, 2457–2471.
- Kistler, R., and Coauthors, 2001: The NCEP–NCAR 50-Year Reanalysis: Monthly means CD-ROM and documentation. *Bull. Amer. Meteor. Soc.*, **82**, 247–268.
- Large, W. G., J. C. McWilliams, and S. C. Doney, 1994: Oceanic vertical mixing: A review and a model with a nonlocal boundary layer parameterization. *Rev. Geophys.*, **32**, 363–403.
- Legeckis, R., and A. L. Gordon, 1982: Satellite observations of the Brazil and Falkland Currents, 1975 to 1976 and 1978. *Deep-Sea Res.*, **29**, 375–401.
- Lindzen, R. S., and S. Nigam, 1987: On the role of sea surface temperature gradients in forcing low-level winds and convergence in the Tropics. *J. Atmos. Sci.*, **44**, 2418–2436.
- Liu, W. T., and W. Tang, 1996: Equivalent neutral wind. Jet Propulsion Laboratory Tech. Rep. 96–17, 20 pp. [Available online at <http://airsea-www.jpl.nasa.gov/data/data.html>.]
- Lutjeharms, J. R. E., and J. M. Meeuwis, 1987: The extent and variability of south-east Atlantic upwelling. *South African J. Mar. Sci.*, **5**, 51–62.
- Maloney, E. D., and D. B. Chelton, 2006: An assessment of the SST influence on surface wind stress in numerical weather prediction and climate models. *J. Climate*, **19**, 2743–2762.
- Mears, C. A., D. K. Smith, and F. J. Wentz, 2001: Comparison of SSM/I and buoy-measured wind speeds from 1987 to 1997. *J. Geophys. Res.*, **106**, 11 719–11 729.
- Mestas-Nuñez, A. M., D. B. Chelton, M. H. Freilich, and J. G. Richman, 1994: An evaluation of ECMWF-based climatological wind stress fields. *J. Phys. Oceanogr.*, **24**, 1532–1549.

- Mignone, B. K., A. Gnanadesikan, J. L. Sarmiento, and R. D. Slater, 2006: Central role of Southern Hemisphere winds and eddies in modulating the oceanic uptake of anthropogenic carbon. *Geophys. Res. Lett.*, **33**, L01604, doi:10.1029/2005GL024464.
- Milliff, R. F., and J. Morzel, 2001: The global distribution of the time-average wind-stress curl from NSCAT. *J. Atmos. Sci.*, **58**, 109–131.
- , W. G. Large, J. Morzel, G. Danabasoglu, and T. M. Chin, 1999: Ocean general circulation model sensitivity to forcing from scatterometer winds. *J. Geophys. Res.*, **104**, 11 337–11 358.
- , J. Morzel, D. Chelton, and M. H. Freilich, 2004: Wind stress curl and wind stress divergence biases from rain effects on OSCAT surface wind retrievals. *J. Atmos. Oceanic Technol.*, **21**, 1216–1231.
- Minobe, S., A. Kuwano-Yoshida, N. Komori, S.-P. Xie, and R. J. Small, 2008: Influence of the Gulf Stream on the troposphere. *Nature*, **452**, 206–209.
- Mitchell, T. P., and J. M. Wallace, 1992: The annual cycle in equatorial convection and sea surface temperature. *J. Climate*, **5**, 1140–1156.
- Moore, G. W. K., 2003: Gale force winds over the Irminger Sea to the east of Cape Farewell, Greenland. *Geophys. Res. Lett.*, **30**, 1894, doi:10.1029/2003GL018012.
- Niiler, P. P., N. A. Maximenko, and J. C. McWilliams, 2003: Dynamically balanced absolute sea level of the global ocean derived from near-surface velocity observations. *Geophys. Res. Lett.*, **30**, 2164, doi:10.1029/2003GL018628.
- Nonaka, M., and S.-P. Xie, 2003: Covariations of sea surface temperature and wind over the Kuroshio and its extension: Evidence for ocean-to-atmospheric feedback. *J. Climate*, **16**, 1404–1413.
- O'Connor, B. M., R. A. Fine, and D. B. Olson, 2005: A global comparison of subtropical underwater formation rates. *Deep-Sea Res.*, **52**, 1569–1590.
- Olson, D. B., G. P. Podesta, R. H. Evans, and O. B. Brown, 1988: Temporal variations in the separation of Brazil and Malvinas currents. *Deep-Sea Res.*, **35**, 1971–1990.
- O'Neill, L. W., D. B. Chelton, and S. K. Esbensen, 2003: Observations of SST-induced perturbations of the wind stress field over the Southern Ocean on seasonal time scales. *J. Climate*, **16**, 2340–2354.
- , —, —, and F. J. Wentz, 2005: High-resolution satellite measurements of the atmospheric boundary layer response to SST variations along the Agulhas Return Current. *J. Climate*, **18**, 2706–2723.
- Pacanowski, R. C., 1987: Effect of equatorial currents on surface stress. *J. Phys. Oceanogr.*, **17**, 833–838.
- Park, K.-A., P. Cornillon, and D. L. Codiga, 2006: Modification of surface winds near ocean fronts: Effects of Gulf Stream rings on scatterometer (QuikSCAT, NSCAT) wind observations. *J. Geophys. Res.*, **111**, C03021, doi:10.1029/2005JC003016.
- Pedlosky, J., 1987: *Geophysical Fluid Dynamics*. Springer-Verlag, 710 pp.
- Peterson, R. G., and L. Stramma, 1991: Upper-level circulation in the South Atlantic Ocean. *Prog. Oceanogr.*, **26**, 1–73.
- Pickart, R. S., M. A. Spall, M. H. Ribergaard, G. W. K. Moore, and R. F. Milliff, 2003: Deep convection in the Irminger Sea forced by the Greenland tip jet. *Nature*, **424**, 152–156.
- Reynolds, R. W., T. M. Smith, C. Liu, D. B. Chelton, K. S. Casey, and M. G. Schlax, 2007: Daily high-resolution-blended analyses for sea surface temperature. *J. Climate*, **20**, 5473–5496.
- Risien, C. M., and D. B. Chelton, 2006: A satellite-derived climatology of global ocean winds. *Remote Sens. Environ.*, **105**, 221–236, doi:10.1016/j.rse.2006.06.017.
- Saenko, O. A., J. C. Fyfe, and M. H. England, 2005: On the response of the oceanic wind-driven circulation to atmospheric CO<sub>2</sub> increase. *Climate Dyn.*, **25**, 415–426, doi:10.1007/s00382-005-0032-5.
- Samelson, R. M., E. D. Skillingstad, D. B. Chelton, S. K. Esbensen, L. W. O'Neill, and N. A. Thum, 2006: On the coupling of wind stress and sea surface temperature. *J. Climate*, **19**, 1557–1566.
- Sampe, T., and S.-P. Xie, 2007: Mapping high sea winds from space: A global climatology. *Bull. Amer. Meteor. Soc.*, **88**, 1965–1978.
- Schlax, M. G., D. B. Chelton, and M. H. Freilich, 2001: Sampling errors in wind fields constructed from single and tandem scatterometer datasets. *J. Atmos. Oceanic Technol.*, **18**, 1014–1036.
- Schott, F. A., and J. P. McCreary Jr., 2001: The monsoon circulation of the Indian Ocean. *Prog. Oceanogr.*, **51**, 1–123.
- , J. Fischer, U. Garternicht, and D. Quadfasel, 1997: Summer monsoon response of the Northern Somali Current, 1995. *Geophys. Res. Lett.*, **24**, 2565–2568.
- Seidov, D., and B. J. Haupt, 2005: How to run a minimalist's global ocean conveyor. *Geophys. Res. Lett.*, **32**, L07610, doi:10.1029/2005GL022559.
- Small, J. R., S.-P. Xie, Y. Wang, S. K. Esbensen, and D. Vickers, 2005: Numerical simulation of boundary layer structure and cross-equatorial flow in the eastern Pacific. *J. Atmos. Sci.*, **62**, 1812–1830.
- Smith, S. D., 1980: Wind stress and heat flux over the ocean in gale force winds. *J. Phys. Oceanogr.*, **10**, 709–726.
- , 1988: Coefficients for sea surface wind stress, heat flux and wind profiles as a function of wind speed and temperature. *J. Geophys. Res.*, **93**, 15 467–15 474.
- , 1989: Water vapour flux at the sea surface. *Bound.-Layer Meteor.*, **47**, 277–293.
- Song, Q., P. Cornillon, and T. Hara, 2006: Surface wind response to oceanic fronts. *J. Geophys. Res.*, **111**, C12007, doi:10.1029/2006JC003680.
- Stiles, B. W., and S. H. Yueh, 2002: Sea surface and winds—Impact of rain on spaceborne Ku-band wind scatterometer data. *IEEE Trans. Geosci. Remote Sens.*, **40**, 1973–1983.
- Stuhne, G. R., and W. R. Peltier, 2006: A robust unstructured grid discretization for 3-dimensional hydrostatic flows in spherical geometry: A new numerical structure for ocean general circulation modeling. *J. Comp. Physics*, **213**, 704–729.
- Sweet, W. R., R. Fett, J. Kerling, and P. LaViolette, 1981: Air-sea interaction effects in the lower troposphere across the north wall of the Gulf Stream. *Mon. Wea. Rev.*, **109**, 1042–1052.
- Tokinaga, H., Y. Tanimoto, and S.-P. Xie, 2005: SST-induced surface wind variations over the Brazil–Malvinas Confluence: Satellite and in situ observations. *J. Climate*, **18**, 3470–3482.
- Trasviña, A., E. D. Barton, J. Brown, H. S. Velez, P. M. Kosro, and R. L. Smith, 1995: Offshore wind forcing in the Gulf of Tehuantepec, Mexico: The asymmetric circulation. *J. Geophys. Res.*, **100**, 20 649–20 663.
- Trenberth, K. E., W. G. Large, and J. G. Olson, 1990: The mean annual cycle in global ocean wind stress. *J. Phys. Oceanogr.*, **20**, 1742–1760.

- Tyson, P. D., and R. A. Preston-Whyte, 2000: *The Weather and Climate of Southern Africa*. 2nd ed. Oxford University Press, 396 pp.
- Urbano, D. F., M. Jochum, and I. C. A. da Silveira, 2006: Rediscovering the second core of the Atlantic NECC. *Ocean Modell.*, **12**, 1–15.
- Vecchi, G. A., S. P. Xie, and A. S. Fischer, 2004: Ocean–atmosphere covariability in the western Arabian Sea. *J. Climate*, **17**, 1213–1224.
- WGASF, 2000: Intercomparison and validation of ocean–atmosphere energy flux fields. Joint WCRP–SCOR Working Group on Air–Sea Fluxes (SCOR Working Group 110) Final Rep. WCRP-112, WMO/TD-No. 1036, WMO, 312 pp.
- WMO, 1993: International list of selected, supplementary and auxiliary ships. WMO Rep. 47, WMO, 406 pp.
- Woodruff, S. D., R. J. Slutz, R. L. Jenne, and P. M. Steurer, 1987: A comprehensive ocean–atmosphere data set. *Bull. Amer. Meteor. Soc.*, **68**, 1239–1250.
- , S. J. Lubker, K. Wolter, S. J. Worley, and J. D. Elms, 1993: Comprehensive Ocean–Atmosphere Data Set (COADS) release 1a: 1980–92. *Earth Syst. Monitor*, **4**, 4–8.
- Worley, S. J., S. D. Woodruff, R. W. Reynolds, S. J. Lubker, and N. Lott, 2005: ICOADS release 2.1 data and products. *Int. J. Climatol.*, **25**, 823–842.
- Xie, S.-P., W. T. Liu, Q. Liu, and M. Nonaka, 2001: Far-reaching effects of the Hawaiian Islands on the Pacific Ocean atmosphere. *Science*, **292**, 2057–2060.
- , X. Haiming, W. S. Kessler, and M. Nonaka, 2005: Air–sea interaction over the eastern Pacific warm pool: Gap winds, thermocline dome, and atmospheric convection. *J. Climate*, **18**, 5–20.